A&A 574, A25 (2015)
DOI: 10.1051/0004-6361/201424229

Astronomy & Astrophysics

Doppler images and the underlying dynamo⋆,⋆⋆,⋆⋆⋆

The case of AF Leporis

S. P. Järvinen[1], R. Arlt[1], T. Hackman[2,3], S. C. Marsden[4], M. Küker[1], I. V. Ilyin[1], S. V. Berdyugina[5], K. G. Strassmeier[1], and I. A. Waite[4]

[1] Leibniz-Institut für Astrophysik Potsdam, An der Sternwarte 16, 14482 Potsdam, Germany
e-mail: sjarvinen@aip.de
[2] Department of Physics, University of Helsinki, PO Box 64, 00014 Helsinki, Finland
[3] Finnish Centre for Astronomy with ESO (FINCA), University of Turku, Väisäläntie 20, 21500 Piikkiö, Finland
[4] Computational Engineering and Science Research Centre, University of Southern Queensland, 4350 Toowoomba, Australia
[5] Kiepenheuer-Institut für Sonnenphysik, Schöneckstr. 6, 79104 Freiburg, Germany

Received 19 May 2014 / Accepted 3 November 2014

ABSTRACT

Context. The (Zeeman-)Doppler imaging studies of solar-type stars very often reveal large high-latitude spots. This also includes F stars that possess relatively shallow convection zones, indicating that the dynamo operating in these stars differs from the solar dynamo.
Aims. We aim to determine whether mean-field dynamo models of late-F type dwarf stars can reproduce the surface features recovered in Doppler maps. In particular, we wish to test whether the models can reproduce the high-latitude spots observed on some F dwarfs.
Methods. The photometric inversions and the surface temperature maps of AF Lep were obtained using the Occamian-approach inversion technique. Low signal-to-noise spectroscopic data were improved by applying the least-squares deconvolution method. The locations of strong magnetic flux in the stellar tachocline as well as the surface fields obtained from mean-field dynamo solutions were compared with the observed surface temperature maps.
Results. The photometric record of AF Lep reveals both long- and short-term variability. However, the current data set is too short for cycle-length estimates. From the photometry, we have determined the rotation period of the star to be 0.9660 ± 0.0023 days. The surface temperature maps show a dominant, but evolving, high-latitude (around +65°) spot. Detailed study of the photometry reveals that sometimes the spot coverage varies only marginally over a long time, and at other times it varies rapidly. Of a suite of dynamo models, the model with a radiative interior rotating as fast as the convection zone at the equator delivered the highest compatibility with the obtained Doppler images.

Key words. stars: imaging – stars: activity – starspots – stars: individual: AF Leb – dynamo

1. Introduction

Solar-type stars form a very broad class of stars from late-F to early-K type dwarfs and sub-giants, all containing a convective envelope over a radiative interior. Observations of these stars provide excellent constraints for theoretical dynamo models. Our understanding of the operation of the magnetic dynamo in such stars is based on the solar case, where the solar activity cycle is believed to be generated through dynamo action operating either in the convection zone or in the stably stratified layer beneath it (for a short overview of solar dynamo models see, e.g., Passos et al. 2014). One would expect stars with an internal structure similar to that of the Sun, that is, stars with convective envelopes, to show the same type of dynamo operation. However, (Zeeman-)Doppler imaging studies frequently find large spots at high latitudes and large regions of a near-surface azimuthal field (not seen on the solar surface). For very active stars, it has been suggested that instead of a solar-like dynamo, which probably works in the overshoot zone, a distributed $\alpha^2\Omega$- or α^2-dynamo is likely to be present (Brandenburg et al. 1989; Moss et al. 1995).

F stars possess relatively shallow convection zones. Nevertheless, observations show via the Doppler imaging method that at least some of these stars have high-latitude and even polar spots (e.g., AF Lep: Marsden et al. 2006; τ Boo: Fares et al. 2009; one of the components in σ^2 CrB: Strassmeier & Rice 2003). Furthermore, surface differential-rotation estimates imply that $\delta\Omega$ increases with decreasing depth of the convection zone (e.g., Marsden et al. 2011b; Barnes et al. 2005a). Theoretical models support this result (e.g., Küker & Rüdiger 2007).

AF Lep (HR 1817, HD 35850) is an active, young, rapidly rotating, single solar-like star. The first photometric observations of the target are from the late 60s (Stokes 1972), and it was also detected with EXOSAT (Cutispoto et al. 1991). It has been identified as a member of the β Pictoris moving group, which has been estimated to have an age of ~20 Myr

⋆ Partially based on observations made with the Nordic Optical Telescope, operated by the Nordic Optical Telescope Scientific Association at the Observatorio del Roque de los Muchachos, La Palma, Spain, of the Instituto de Astrofísica de Canarias.
⋆⋆ Based partly on STELLA SES data.
⋆⋆⋆ Tables 1–3 and Figs. 7–14 are available in electronic form at http://www.aanda.org

(Fernández et al. 2008 and references therein; Binks & Jeffries 2014; Mamajek & Bell 2014). The colours suggest a spectral classification of F8/9 (Cutispoto et al. 1996). The high Li abundance (log N(Li) = 3.2), solar metallicity, and high rotation velocity ($v \sin i$ = 50 km s^{-1}) are consistent with the star being a young object. Furthermore, it has an unusually high intrinsic X-ray luminosity of $\sim 1.6 \times 10^{30}$ ergs s^{-1} for a single, late-F-type star (Tagliaferri et al. 1994).

The first photometric monitoring of the star by Cutispoto et al. (1996) did not reveal photometric variability. However, the flat-bottomed shapes of Stokes I line intensity profiles suggested that a dark spot is present on AF Lep (Budding et al. 2002). Later, a photometric follow-up revealed a prominent photometric minimum in a phase diagram (Budding et al. 2003).

This paper has two parts. In the first part, we explore what we can learn about AF Lep via photometric and spectroscopic observations. The second part of the paper consists of theoretical calculations aiming to determine whether high-latitude spots can be formed.

2. Observations and data reduction

2.1. Photometric observations

We started to observe AF Lep in March/April 2010 with the *Amadeus*, a T7 Automatic Photoelectric Telescope (APT) at Fairborn Observatory, jointly operated by the University of Vienna and Leibniz-Institute für Astrophysik Potsdam (AIP), with Johnson-Cousins V filter (for more details see Strassmeier et al. 1997b). After that, four additional data sets were obtained (see Fig. 1). During the first observing run the star was observed from four to nine times per night for a month. The subsequent runs lasted longer – from four to five months – but the star was observed less frequently, and there are only one or two data points per night. Measurements were made differentially between the target, a comparison star (HD 36379), a check star (HD 34538), and the sky position. The data reduction is automated and was described by Strassmeier et al. (1997a) and Granzer et al. (2001a).

2.2. Spectroscopic and spectropolarimetric observations

Most of the spectroscopic and spectropolarimetric observations of AF Lep were carried out during two simultaneous observing runs with the fibre-fed STELLA Echelle Spectrograph (SES) mounted on STELLA-I (Tenerife; Strassmeier et al. 2004; Granzer et al. 2001b) and the Anglo-Australian Telescope (AAT) with the SEMPOL visiting polarimeter (Semel et al. 1993; Marsden et al. 2011a) during December 2008 and November/December 2009. The STELLA observations were also continued into January 2010. Furthermore, AF Lep had been observed earlier in November 2005 with SOFIN at the Nordic Optical Telescope (NOT, La Palma). The STELLA data have a continuous wavelength coverage (3900–9000 Å) with a resolving power of 55 000. The spectra from the AAT have a shorter wavelength coverage (4380–6810 Å) but higher resolution (~70 000). The SOFIN échelle spectrograph, acquired with the second camera, provides 33 useful orders in a spectral range of 3930–9040 Å. The slit width of 65 μm centred at 6427 Å gives a resolution of 76 000. More information is presented in Tables 1–3.

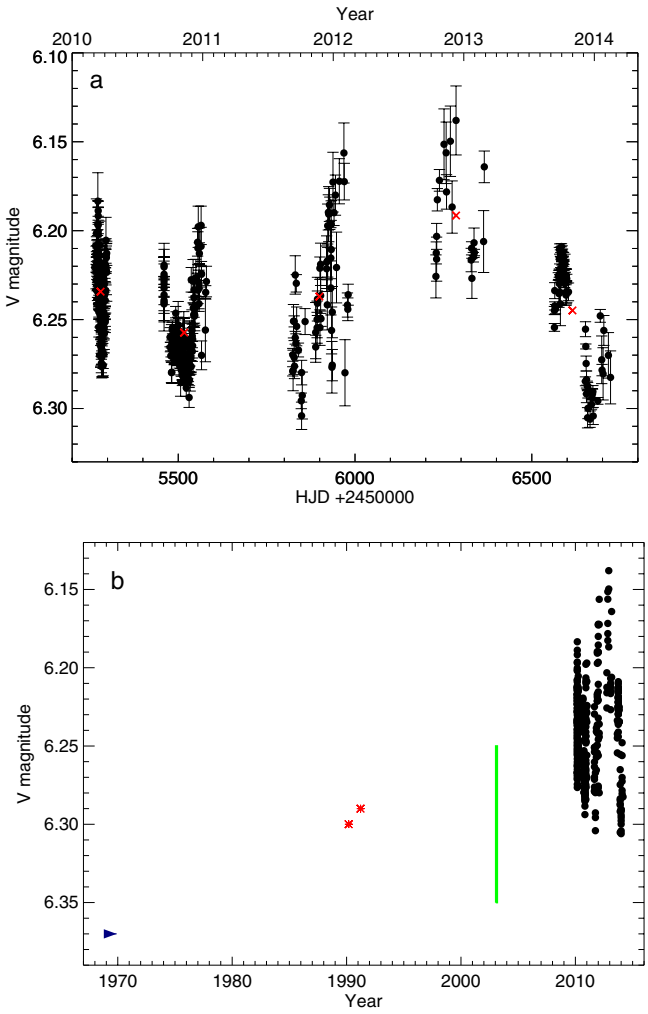

Fig. 1. a) V-band photometric data of AF Lep with measurement errors used in this paper. The mean value of each observing season is plotted with red x. **b)** The whole photometric record in the V-band: the blue arrowhead represents data from Stokes (1972), the red asterisks data from Cutispoto et al. (1996), the green bar illustrates the magnitude range from Budding et al. (2003), and black dots represent this work.

3. Determining the rotation period

As summarised by Silva-Valio (2008), for example, there are two methods that are used to determine a rotation period of a star. One uses rotational broadening of spectral lines. This method, however, is usable only for stars that rotate faster than a threshold velocity set by the spectral resolution and has always sin i uncertainty, i being the inclination of a star. Furthermore, it gives an average of the periods of the whole stellar disk. The other method uses the periodic modulation of the stellar flux due to the co-rotating dark and bright features on the stellar surface. The advantages of this method are that it can also be used for stars with long periods, it is only mildly affected by latitudinal differential rotation, and the obtained period corresponds to the period of the latitudes where these features are. However, normally, the information on the latitudes of stellar active regions cannot be extracted from a one-dimensional data set, that is, a light-curve. Lately, starspot detections during planetary transits are also used for estimating rotation periods that represent periods at specific latitudes (see Silva-Valio 2008).

Lanza (2011) discussed differences in the spot distribution of the Sun and active stars. On the Sun, the active regions are a

mixture of cool spots and bright faculae that evolve on different timescales. However, in very active stars, the cool spots probably dominate the variation. And not only that, but the optical variability of the Sun is dominated by several active regions at the same time. One has to keep in mind that sunspots and solar active regions have typical lifetimes of days to weeks (Solanki 2003), whereas starspots have been observed to persist over a long time (e.g., Strassmeier 2009).

Co-rotating spots on the surface, pulsations, spot evolution, instrumental effects, and a combination of all of them can introduce periodic variations in the light curves. Despite these effects, light curves often show notable stability in the phase, shape, and amplitude of photometric variability over long times. Meibom et al. (2011) discussed the two possible explanations for this: either the spots are longer-lived than the sunspots, or they tend to emerge non-uniformly at preferred long-lived active longitudes. The outcome from the first scenario was that although on the Sun the lifetime of the spots increases linearly with area, and the solar log-normal spot distribution is strongly dominated by small spots, there is no evidence that the log-normal distribution holds for other stars. However, on other stars the small spots dominate as well, although they are very often unresolved (see, e.g., Lanza et al. 2009; Silva-Valio et al. 2010). Furthermore, lifetimes of individual starspots can be short (Mosser et al. 2009), but the large-scale spot groups can live long (Hussain 2002). The second possibility was that starspots emerge at preferred longitudes. Here it is assumed that the spots seen in photometry and in Doppler images are not huge individual spots, but rather spot groups consisting of a range of smaller spots emerging at preferred longitudes. This could lead to obtaining observed spottedness over longer periods of time although individual spots come and go. As Meibom et al. (2011) stated, the only requirement is that the emergence rate is high enough to maintain a rather stable spot coverage, but this is expected for young and active stars.

The rotation period of AF Lep has commonly been reported to be around one day: Budding et al. (2003) used $P = 1\overset{\mathrm{d}}{.}0$ for phasing photometry and Marsden et al. (2006) reported a period of $\sim 1\overset{\mathrm{d}}{.}0$ from spectroscopy. This is notoriously near the typical window of ground observations ($P_0 = 0\overset{\mathrm{d}}{.}9972$), which creates challenges for determining the period from ground-based photometry. To achieve a good phase coverage using a single telescope, observations covering a long time-base are needed, which in turn may mean that the surface features (and thus the light curve) have undergone significant changes during this time. We can also expect significant problems with spurious periods very near the real one.

We applied time-series analysis methods to the March/April 2010 photometry set (Fig. 1a). Using the Lomb method for unevenly sampled data (Press et al. 1992), we detected a prominent double peak corresponding to periods of $0\overset{\mathrm{d}}{.}97$ and $1\overset{\mathrm{d}}{.}03$ (Fig. 2). Using the method described by Jetsu & Pelt (1999), we estimated that the probability of $1\overset{\mathrm{d}}{.}03$ being a real period was 4×10^{-6}, while $0\overset{\mathrm{d}}{.}97$ passed the test of being non-spurious. This method uses bootstrapping for the model parameter error estimates, evaluates the modelling statistics with the Kolmogorov-Smirnov test, and identifies spurious periodicities from real ones with the phase residual regression. We then applied the continuous-period search method (Lehtinen et al. 2011), which accounts for changing spot patterns, using a window length ($\Delta T_{\max}$) covering the whole data set. In practice, this meant fitting the model

$$y_{\mathrm{cps}}(t_i, \bar{\beta}) = a_0 + \sum_{k=1}^{K} \left[a_k \cos(2\pi k f t_i) + b_k \sin(2\pi k f t_i) \right] \quad (1)$$

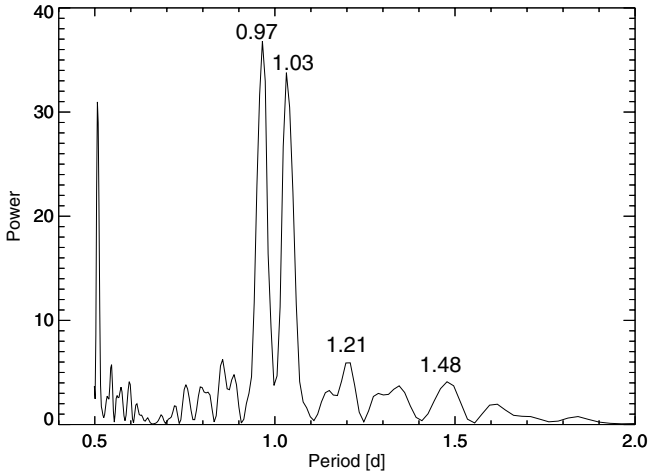

Fig. 2. Lomb-periodogram showing possible rotation periods.

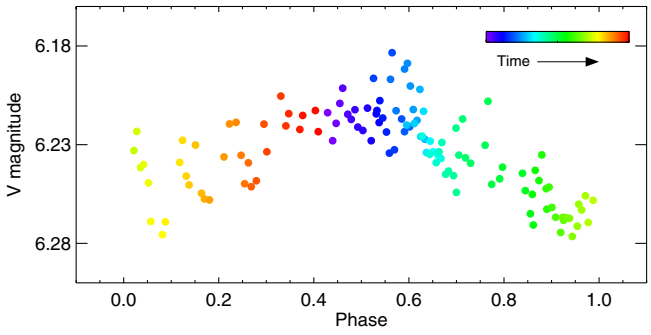

Fig. 3. Phase diagram for the period $P_{\mathrm{phot}} = 0.9660$ using the March/April 2010 data set. The observations cover 30 days and the data points have been colour-coded with increasing time of observations.

to the observations (y). Here a_0, a_k, b_k and $f = 1/P_{\mathrm{phot}}$ are free parameters and t_i the times of the observations. With the optimal order $K = 1$, we obtained the period $P_{\mathrm{phot}} \approx 0\overset{\mathrm{d}}{.}9660 \pm 0\overset{\mathrm{d}}{.}0023$ and the time of the first photometric minimum $\mathrm{HJD}_0 = 2\,455\,268.227 \pm 0.039$. Thus we used the ephemeris

$$\mathrm{HJD}_{\mathrm{min}} = 2\,455\,268.227 + 0.9660E, \quad (2)$$

to derive the rotation phases for our photometric and spectroscopic data. The phase diagram using this ephemeris for the March/April 2010 photometry is displayed in Fig. 3.

4. Photometric variability

The collected photometry shows both long- and short-term variability. Moreover, if we compare the measured values presented in Fig. 1a with the first reported V magnitude of 6.37 (Stokes 1972), one can conclude that the spot coverage has been larger in the past. The observed magnitudes can also be compared with magnitudes from the early 90s ($V = 6.30$ and 6.29; Cutispoto et al. 1996), which were on the level of our faintest data points. The photometry from 2003 ($V = 6.35$–6.25; Budding et al. 2003) shows that the mean brightness has slowly increased over the past 40 years to the values presented here. The whole photometric record (Fig. 1b) implies that AF Lep might have a long-term trend, and our four years of observations indicate that there is also variability on shorter timescales, although the data set

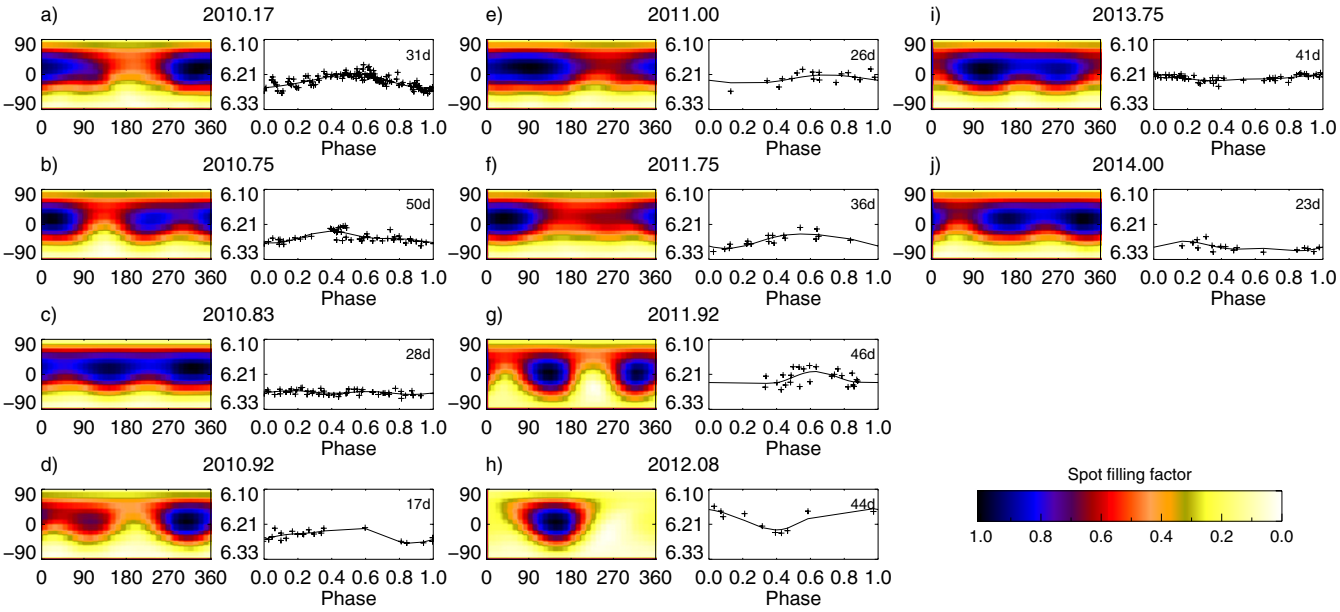

Fig. 4. Each data subset (**a**–**j**) is visualised with two images. The given times represent the middle point of each set. *On the left*, we show the light-curve inversion result. The spot-filling factor is larger in the darker regions. A light curve represents a one-dimensional time series and, therefore, the resulting stellar image contains information on the spot distribution only in longitudinal direction. *On the right*, the observed and calculated V-band magnitudes are plotted with crosses and lines, respectively. The length of the set (in days) is given in the upper right corner.

is not long enough to obtain a reliable cycle length estimate. However, a local minimum occurred around mid-2011, a local maximum was reached around 2012/2013, and in early 2014 the star was dimmer again. Furthermore, the amplitude of the brightness variations implies rotational modulation due to changing spot coverage.

To analyse the short-term variability in detail, we inverted the light curves into stellar images (for details about the method, see Berdyugina et al. 2002). As seen from Figs. 3 and 4a, from March/April 2010 it is possible to obtain a smooth light curve, where the data points from the beginning of the observing season match those obtained at the end of the season with the obtained period. However, the amplitude of the night-to-night variations is relatively large. In this subset, the spots are concentrated around phase $\varphi = 0.0$. However, the second data set (August 2010–January 2011), shows significant short-term variations and can be divided into four subsets (Figs. 4b–e). These sets show moderate phase migration, and a secondary minimum appears in the light curves (Figs. 4b–d). A new subset was started when a clear change in the photometric behaviour was detected, that is, a real break in the observations, or when the subsequent data points started to form a maximum instead of a minimum. Variability is also present in later data sets, although observations are rather infrequent and, therefore, it is not always possible to create a continuous light curve over all phases (see Fig. 4g), where observations covering 46 days have large scatter and a gap of 0.4 in phase. The photometric minimum is often rather broad, which agrees with high-latitude spots (see Sect. 5) and the inclination of the star.

The drifting of the spot longitudes around $\varphi = 0.0$ may be due to an error in the period, which is not easy to determine in this case, as discussed in Sect. 3. An alternative explanation might be a significant surface differential rotation. Using Zeeman-Doppler imaging with Stokes V-profiles, Marsden et al. (2006) derived values of $\Omega_{\rm eq} = 6.495 \pm 0.011$ rad d^{-1} and $\delta\Omega = 0.259 \pm 0.019$ rad d^{-1} for AF Lep. The third option might be drifting due to an azimuthal dynamo wave (Cole et al. 2014), although we recall that it is a competitive mechanism to the differential rotation, and the drift could be due to a combination of them.

5. Surface spot configuration

The spectroscopic observations were phased with the derived new ephemeris (Eq. (2)). Local line profiles were calculated with the code of Berdyugina (1991). This includes calculating the opacities in the continuum and in atomic and molecular lines, although in this paper molecular lines were omitted. Atomic line parameters were obtained from the Vienna Atomic Line Database (VALD; Piskunov et al. 1995; Kupka et al. 1999). The stellar model atmospheres used here are from Kurucz (1993). The local line profiles were calculated for 20 values of $\mu = \cos\theta$ from the disk centre to the limb. The spectra were calculated for temperatures ranging from 4000 K to 6500 K in steps of 250 K. The Occamian approach was used to invert of the observed line profiles into stellar images (Berdyugina 1998). A $6° \times 6°$ grid on the stellar surface was used to integrate local line profiles into normalised flux profiles. With a set of stellar atmosphere models, the stellar image is considered as the distribution of the effective temperature across the stellar surface, as is commonly done in Doppler imaging. This code does not take differential rotation into account. The stellar parameters used are presented in Table 4.

The noise in both STELLA and AAT data was reduced using the least-squares deconvolution (LSD) technique (see Semel 1989 and Donati et al. 1997 for the algorithm; and Järvinen & Berdyugina 2010 for the application). For this purpose, a line mask containing 93 spectral lines was built using lines within a wavelength range of 4770–6900 Å. They are mainly Fe I, Ni I, and Ca I lines. This gives a boost from signal-to-noise ratio $S/N = 100$ to $S/N = 230$ and from $S/N = 150$ to $S/N = 320$. From the SOFIN data, the surface temperature map was inverted using three spectral lines: Fe I 6411.64 Å, Fe I 6430.80 Å, and Ca I 6439.08 Å.

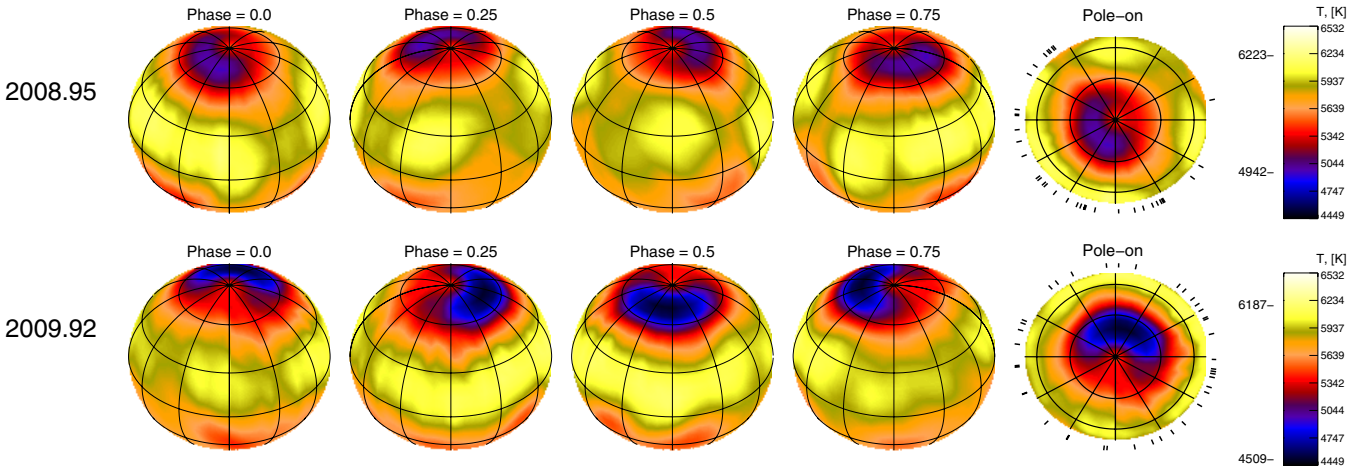

Fig. 5. Temperature maps of AF Lep from the data sets with a good phase coverage. They were obtained by combining simultaneous AAT and STELLA observations. For both seasons the map is shown from four angles and pole-on. The used phases have been marked with ticks around the pole-on projection. All maps have a common temperature scale, and the highest and lowest temperature of each map is shown at the left side of the temperature scale.

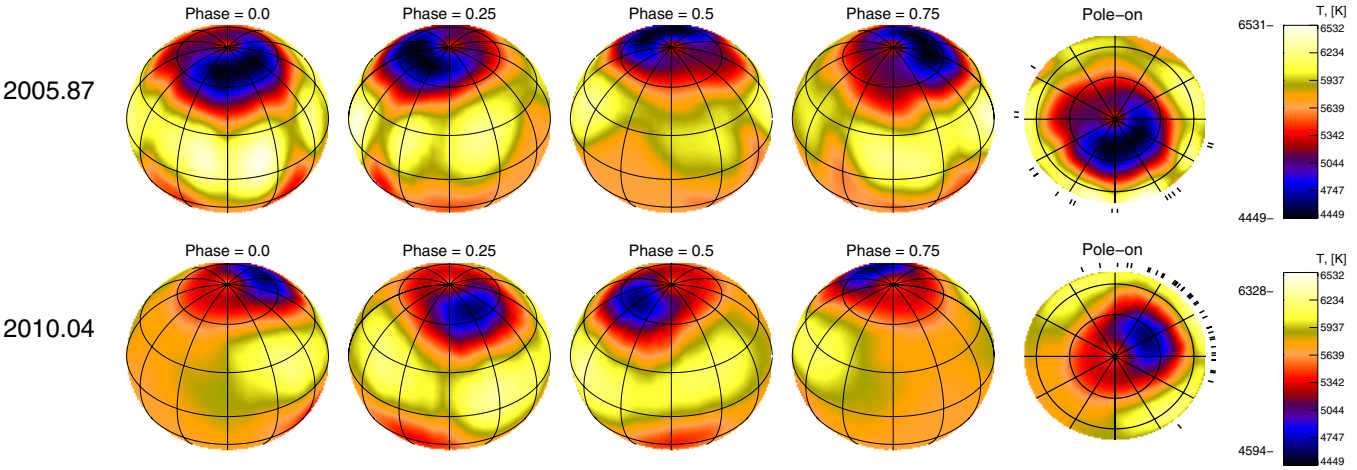

Fig. 6. Temperature maps of AF Lep from the data sets with an incomplete phase coverage. The 2005 data set was obtained at the NOT, the 2010 data set with STELLA. Otherwise maps as in Fig. 5.

Table 4. Stellar parameters of AF Lep with references.

Parameter	Value	Ref.
Sp. type	F8 V	1
$T_{\rm eff}$	6100 K	2
log g	4.4	2
log n(Li)	3.2	2
$B-V$	0.55	2,3
$v \sin i$	50 km s^{-1}	2
inclination	50°	4
Mass	1.15 $M_\odot$	5
Radius	1.18 $R_\odot$	6
Period	$0\overset{\rm d}{.}9660$ d	7

References. (1) Eggen (1986); (2) Tagliaferri et al. (1994); (3) Cutispoto et al. (1996); (4) Marsden et al. (2006); (5) Kim & Demarque (1996); (6) Blackwell & Lynas-Gray (1994); (7) this work.

The resulting temperature maps are shown in Figs. 5 and 6. The fits to the observed spectra and LSD profiles are shown in Figs. 7–10 and the differences between the mean profile and the observed ones are illustrated in Figs. 11–14 to visualise spots moving through the line profiles. To create the temperature map from 2005 observations, all available individual SOFIN observations were used. For the other temperature maps, mainly the SEMPOL spectra from the AAT were used because it gives the best phase coverage, and the long phase-gaps were filled using the STELLA spectra. For the spectropolarimetric SEMPOL observations there are four consecutive Stokes I exposures for each Stokes V exposure that were added together. The photospheric temperature of 6200 K agrees with earlier results and the spectral type of the star. A cool spot is located near the polar region of the star. The time separation of the maps in Fig. 5 is one year. Although the total spot coverage has seemingly changed very little, clear evolution is detected. In the first map (2008.95) the spot is formed from two components at $\varphi = 0.77$ (secondary) and at $\varphi = 0.96$ (primary). In the latter map (2009.92), the spot has grown larger and the two components now have equal sizes and form a larger spot that covers half of the polar longitudes. The middle point is at $\varphi = 0.47$ and the spot is also cooler. The mean latitude of the spot is around +65°.

The maps presented in Fig. 6 have to be interpreted with care because of the large phase gaps in both data sets – in the first map phases $\varphi = 0.65$–0.21 are covered, and the later map covers only

Table 5. Overview of spot latitudes in comparable targets sorted according to the spectral type of the stars.

Star	Sp. type	P_{rot}	Spots	Note	Ref.
τ Boo[a]	F7 V	$3\overset{d}{.}31$	L-H		1–3
AE Phe B	F8 V	$0\overset{d}{.}3624$	L-M, (P)	B	4–6
σ^2 CrB A	F9 V	$1\overset{d}{.}157$	H,P	B	7
HD 307938	G2 V	$0\overset{d}{.}5641$	(L)-P		8, 9
LQ Lup	G2V-IV	$0\overset{d}{.}31$	(L)-P		10
HII 3163	K0 V	$0\overset{d}{.}414$	L, P		11
AB Dor	K0 V	$0\overset{d}{.}5148$	L-P		12–22
HII 686	K4 V	$0\overset{d}{.}3624$	L,M,P		11
LO Peg	K5-7 V	$0\overset{d}{.}4236$	(L)-P		23–25

Notes. In the "Spots" column P = polar, H = high-latitude, M = mid-latitude, and L = low-latitude. Parenthesis around the letter are used when spots are not always present in that latitude range or are weak. The binarity is stated in the "Note" column with "B". [(a)] Only Zeeman-Doppler imaging maps, no brightness, spot occupancy, nor temperature maps.

References. (1) Catala et al. (2007); (2) Donati et al. (2008); (3) Fares et al. (2009); (4) Maceroni et al. (1991); (5) Maceroni et al. (1994); (6) Barnes et al. (2004); (7) Strassmeier & Rice (2003); (8) Marsden et al. (2004); (9) Marsden et al. (2005); (10) Donati et al. (2000); (11) Stout-Batalha & Vogt (1999); (12) Kürster et al. (1994); (13) Collier-Cameron & Unruh (1994); (14) Collier Cameron (1995); (15) Unruh et al. (1995); (16) Hussain et al. (1997); (17) Unruh & Collier Cameron (1997); (18) Donati & Collier Cameron (1997); (19) Donati et al. (1999); (20) Collier Cameron et al. (1999); (21) Donati et al. (2003); (22) Jeffers et al. (2007); (23) Lister et al. (1999); (24) Barnes et al. (2005b); (25) Piluso et al. (2008).

phases φ = 0.11–0.55. In the 2005.87 map the main feature is at φ = 0.00 with a tail, which has a mid-point at φ = 0.18. In the 2010.04 map the spot is again smaller with the mean phase of φ = 0.35. This map also has the lowest spot latitude (+61°). However, when taking into account the spatial resolution of the maps, the mean latitude of the spots remains relatively constant. The maps inverted from the data with an incomplete phase coverage have a broader temperature range than the maps inverted from the data with a good phase coverage.

The high-latitude spot is anti-symmetric around the polar region in all the maps, and there are no low-latitude features. In this sense the maps presented here differ from the (~2002.00) map by Marsden et al. (2006), which shows a very compact polar (completely above latitude +75°) spot and some very weak low-latitude features.

To validate the obtained results, the spot configuration on AF Lep should be compared with spot configurations on other F dwarfs and with spot configurations on other fast-rotating ($P \leq 1$ d) dwarfs. Unfortunately, there are not many F dwarfs that have been mapped to date. A short overview of the current knowledge about the spot configuration in comparable stars is presented in Table 5. Some binary components are included as well, although they do not make good comparisons because they are very different entities. More comparison targets can be found in an extensive list of Strassmeier (2009).

High-latitude spots are thus common features in rapidly rotating dwarfs, and sometimes the maps show the whole polar region to be covered with spots. A more interesting aspect than how these high-latitude/polar spots can be formed would be whether low-latitude spots are detected or not. However, we recall that the maps have been made and visualised using different techniques. Therefore, it is difficult to judge how prominent the low-latitude features are. Furthermore, low-latitude features appear often less resolved as a result of lower spatial resolution. The simulations show that the places of the spots (or spot groups) are correct, but the temperature contrast suffers from the lack of resolution.

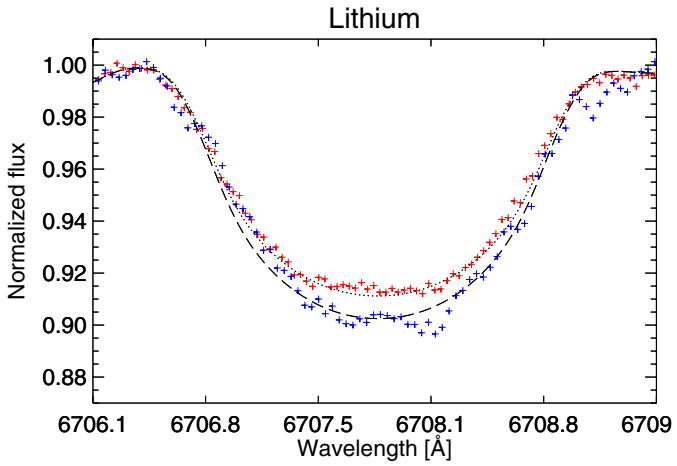

Fig. 15. Mean lithium-line profiles for the 2008 (red) and 2010 (blue) observations. For comparison, we have plotted synthetic spectra calculated using $\log N(\mathrm{Li}) = 3.25$ (dotted line) and $\log N(\mathrm{Li}) = 3.35$ (dashed line), assuming a fixed temperature in the model calculations.

6. Lithium abundance

Tagliaferri et al. (1994) have reported a lithium abundance of $\log N(\mathrm{Li}) = 3.2$ for AF Lep. Our 2005 observations do not cover the lithium line, but for the later observations this region is covered. We determined the lithium-line equivalent width for all individual spectra listed in Tables 1 and 2. To do this, we fitted a double Gaussian to the Li I 6707.8 Å line and the nearby Fe I 6707.4 Å line. Although this is still a combined equivalent width of ^{6}Li and ^{7}Li, the Fe blend is effectively removed. Generally, during 2008 the equivalent width of the lithium line was measured to be smaller than in 2009 or 2010. A clear difference is seen in the mean lithium-line profiles (Fig. 15). As expected (see, e.g., Pallavicini et al. 1993; Cutispoto 2002), the seasonal equivalent-width variations do not show any clear correlation with the phases of the spots. An excellent review of the relationship between spots and lithium equivalent width variations is given by Fekel (1996).

To determine the lithium abundance, we calculated synthetic line profiles, including both atomic and CN line blends. The abundance best fitting the 2008 data is $\log N(\mathrm{Li}) = 3.25$, while $\log N(\mathrm{Li}) = 3.35$ best describes data from both 2009 and 2010 (see Fig. 15) when the temperature is kept constant. The alternative is that the lithium abundance remains constant and the changes detected are due to overall temperature fluctuations. The model grid has temperatures in 250 K steps, and already one step down results in deeper line profiles than any of the observed ones. As Fig. 15 illustrates, the deformation of the lithium line is stronger in 2010 than in 2008. This agrees with the temperature maps, which show that the spot is larger and cooler in 2010 – although we recall that the phase coverage during 2010 is incomplete. The derived values agree well with the result by Tagliaferri et al. (1994), implying that AF Lep is a young object. Furthermore, the literature gives varying values for the equivalent width (EW) of the lithium line on AF Lep. For example, Wichmann et al. (2003) reported EW = 191 mÅ, while White et al. (2007) reported EW = 135 mÅ. The values

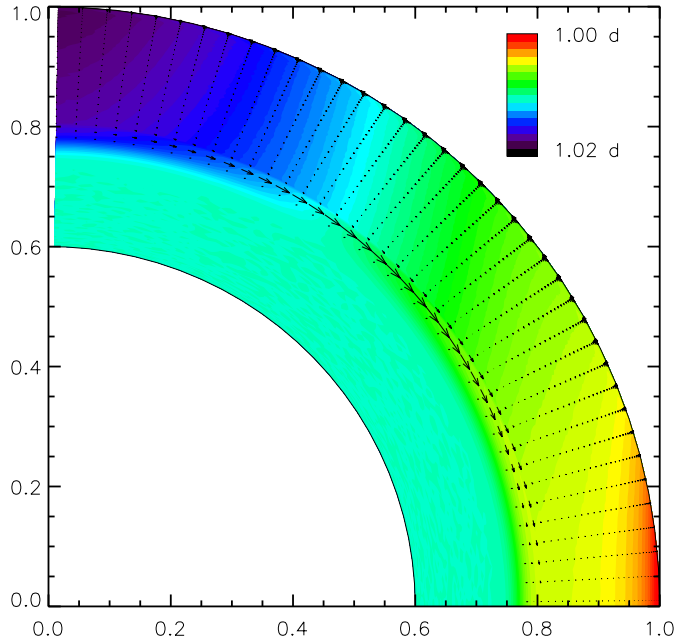

Fig. 16. Rotation profile and meridional circulation from the Λ-effect model in the vertical cross-section of the computational domain, assuming that the core rotation is the average angular velocity between equator and pole at the bottom of the convection zone. Note that the shear layer near $0.8R_*$ is not an artefact but the result of the Λ-effect model.

obtained by Mentuch et al. (2008) and Weise et al. (2010) are in between, EW = 146 mÅ and EW = 149 mÅ, respectively. The mean profile of the 2008 observations has an equivalent width of 160 mÅ, while the corresponding value from 2010 mean profile is 182 mÅ.

7. Dynamo solutions

7.1. Dynamo setup

The aim of this section is to use the theoretical results for the differential rotation and meridional circulation computed for a star of 1.2 $M_\odot$ in a kinematic dynamo model to study whether we can produce a theoretical butterfly diagram that is comparable with the observed spot locations. We chose a spherical shell with r, θ, and ϕ being the radius, colatitude, and azimuth, and placed the inner boundary at 60% of the stellar radius R_* (which is well within the radiative interior of a late-F star), while the outer radius is the stellar surface. The velocity is a vector field $\boldsymbol{u}$, constant in time, containing the theoretical differential rotation and meridional circulation of the star (see, e.g., Fig. 16). They were obtained independently from a mean-field hydrodynamic model employing the Λ-effect and the baroclinicity emerging in rotating, stratified turbulence (Rüdiger 1989; Küker et al. 1993; Kitchatinov et al. 1994; Kitchatinov & Rüdiger 2005). A comparison of a large set of differential rotation parameters obtained for low-mass stars from the *Kepler* mission (Reinhold et al. 2013) and the theoretical predictions by the Λ-effect theory (Küker & Rüdiger 2011) shows a fair agreement and gives us confidence in applying the method to a particular, observed star.

The other effect of rotating, stratified turbulence is the α-effect, which gives rise to a turbulent (averaged) electromotive force, generating poloidal magnetic fields from toroidal ones, and vice versa (Krause & Rädler 1980). The existence of this net effect has been debated recently and may require the removal of small-scale magnetic helicity from the stellar convection zone (Blackman & Brandenburg 2003; Warnecke et al. 2011). We did not consider the exterior here and assumed that it grants the existence of the α-effect.

We solved the induction equation in the mean-field formulation with an α-effect,

$$\frac{\partial \boldsymbol{B}}{\partial t} = \nabla \times \left(\boldsymbol{u} \times \boldsymbol{B} + \boldsymbol{\alpha}(r, \theta, B^2) \circ \boldsymbol{B} - \frac{1}{2}(\nabla \eta_\mathrm{T}) \times \boldsymbol{B} \right) - \nabla \times \eta_\mathrm{T} \nabla \times \boldsymbol{B}, \tag{3}$$

where $\boldsymbol{B}$ is the large-scale magnetic field and $\boldsymbol{u}$ is a given velocity field. The equation also includes diamagnetic pumping, which is a result of a gradient in the turbulent velocities and often neglected in mean-field dynamos. Whenever a gradient in the turbulent magnetic diffusivity η_T is implemented, a variation of the turbulence intensity is implied and requires treatment of the diamagnetic pumping (Krause & Rädler 1980; Kitchatinov & Olemskoy 2012).

The radius of the star R_* and η_T are used to normalise the induction equation, which then modifies to

$$\frac{\partial \hat{\boldsymbol{B}}}{\partial t} = \nabla \times \left(C_\Omega \hat{\boldsymbol{u}} \times \hat{\boldsymbol{B}} + C_\alpha \psi(\hat{B}^2) \hat{\boldsymbol{\alpha}}(\hat{r}, \theta) \circ \hat{\boldsymbol{B}} - \frac{1}{2}(\nabla \hat{\eta}_\mathrm{T}) \times \hat{\boldsymbol{B}} \right) - \nabla \times \hat{\eta}_\mathrm{T} \nabla \times \hat{\boldsymbol{B}}, \tag{4}$$

where we also split the α-tensor into a spatially varying part and a part depending on B^2, since they are (assumed to be) independent. The resulting dimensionless parameters are $C_\Omega = R_*^2 \Omega_\mathrm{eq}/\eta_\mathrm{T}$ and $C_\alpha = R_* \alpha_0/\eta_\mathrm{T}$, with Ω_eq being the equatorial surface angular velocity and α_0 the maximum α-effect in the star in m/s.

For better legibility, we omit all hats from the normalised quantities of r, $\boldsymbol{u}$, $\boldsymbol{B}$, α, and η in the following. In general, $\boldsymbol{\alpha}$ is a tensor of which our α-term contains the symmetric part, while the antisymmetric part is represented by the diamagnetic pumping term, with all three distinct elements of the latter being equal to $-\nabla\eta/2$. The six distinct tensor elements of $\boldsymbol{\alpha}$ for fast rotation (anisotropic α-effect) are

$$\alpha_{rr} = f(r) \cos\theta (1 - 2\cos^2\theta),$$

$$\alpha_{\theta\theta} = f(r) \cos\theta (1 - 2\sin^2\theta),$$

$$\alpha_{\phi\phi} = f(r) \cos\theta,$$

$$\alpha_{r\theta} = 2 f(r) \cos^2\theta \sin\theta, \quad \text{and}$$

$$\alpha_{r\phi} = \alpha_{\theta\phi} = 0;$$

$$f(r) = \frac{1}{2}\left[1 + \mathrm{erf}\left(\frac{r - r_\mathrm{cz}}{d}\right)\right], \tag{5}$$

where $r_\mathrm{cz} = 0.8$ is the bottom radius of the convection zone and $d = 0.02$ is the thickness of the transition to the radiative interior, motivated by the results for the solar tachocline (e.g., Antia & Basu 2011). The convection-zone thickness is based on a stellar model of a 1.2 $M_\odot$ ZAMS star with solar metallicity, computed with the MESA stellar evolution code (Paxton et al. 2011). The quenching function $\psi(B^2)$ represents the suppression of the turbulence by large-scale magnetic fields (Brandenburg et al. 1989), that is, the strength of the α-effect, and is defined as

$$\psi(B^2) = \frac{1}{1 + B^2/B_\mathrm{eq}^2}. \tag{6}$$

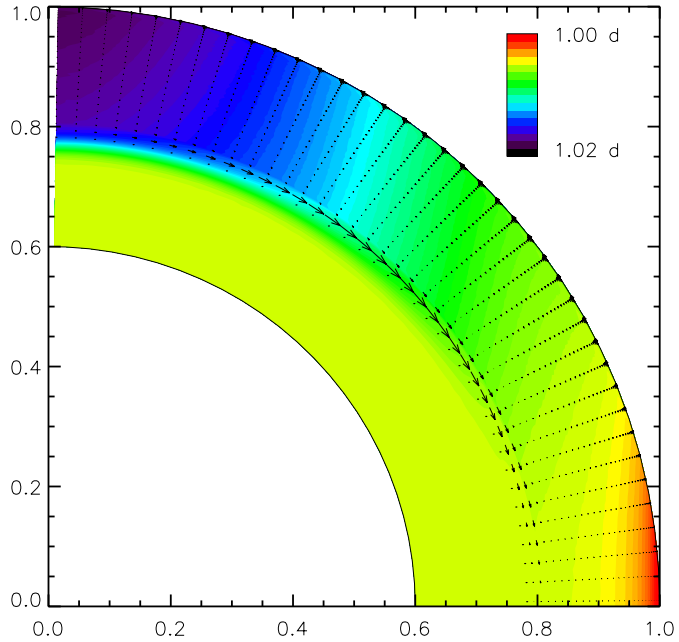

Fig. 17. Modified rotation profile with an interior rotating as fast as the bottom of the convection zone at the equator. The meridional circulation is the same as in Fig. 16.

The magnetic field at which the α-effect drops significantly is the equipartition field strength, $B_{\rm eq} = \sqrt{\mu_0 \rho}\, u_{\rm rms}$, where μ_0 is the permeability constant, ρ the gas density, and $u_{\rm rms}$ the root-mean-square convective velocity.

The magnetic diffusivity in the radiative interior is much lower than the turbulent diffusivity in the convection zone. We employ an arbitrary function for the non-dimensional diffusivity,

$$\eta_{\rm T} = \eta_{\rm core} + \frac{\eta_{\rm cz} - \eta_{\rm core}}{2}\left[1 + {\rm erf}\left(\frac{r - r_{\rm cz}}{d}\right)\right], \quad (7)$$

where $\eta_{\rm core} = 0.01$ is the diffusivity in the interior and $\eta_{\rm cz} = 1$ is the turbulent value in the convection zone.

Assuming $R_* = 1.1\ R_\odot$, $P = 1.0$ days, and a turbulent diffusivity of $\eta_{\rm T} = 10^{12}$ cm^2/s, we obtain a magnetic Reynolds number of $C_\Omega = 4.09 \times 10^5$. The meridional flow obtained in conjunction with the differential rotation is $u_{\rm m} = 48$ m/s, giving a flow Reynolds number of 363.1.

The bottom boundary conditions at $r = 0.6$ for the magnetic field correspond to perfect conductor conditions, while the top boundary at $r = 1$ has exactly vacuum conditions. The mean-field induction Eq. (4) is solved with the numerical code by Hollerbach (2000). As already indicated, we read the velocity field $\boldsymbol{u} = (u_r(r,\theta), u_\theta(r,\theta), u_\phi(r,\theta))$ from the output of the Λ-effect model for the convection zone. In the latter, the boundary conditions for the flow model were stress-free at the stellar surface and at the bottom of the convection zone. Note that this is not the bottom boundary of the dynamo model. Since the computational domain for the dynamo is larger, the differential rotation was extrapolated to sharply change to a uniform rotation in the radiative interior (as we know it does in the Sun). The choice of the rotation rate of the interior is free in principle, so we chose two cases: one takes the Ω of mid-latitudes in the convection zone, the other uses the equatorial Ω of the convection zone. The theoretical rotation patterns $\Omega(r,\theta)$ for AF Lep are illustrated in Figs. 16 and 17.

7.2. Results

The minimum C_α for a growing antisymmetric (dipole-like) solution is 0.20, while it is 1.05 for the symmetric (quadrupole-like) solution. Since magnetic fields suppress the turbulence whence the α-effect (quenching), the effective α-effect is reduced to its lowest marginal value in any place where fields grow. A symmetric solution is therefore very unlikely in AF Lep. We concentrate on antisymmetric solutions in the following. For the estimated magnetic Reynolds number of $C_\Omega = 4.09 \times 10^5$, both antisymetric and symmetric solutions are stationary. Strong meridional circulation can change the oscillatory behaviour of the solutions into stationary ones (Küker et al. 2001).

The latitudinal distribution of the azimuthal magnetic field at the tachocline and the radial field at the surface are plotted over time in Fig. 18. The plot for the tachocline fields is motivated by the concept that the strong shear at the base of the convection zone generates strong azimuthal fields that eventually become buoyantly unstable and rise to the surface to form spots (not modelled here). The largest tachocline fields reside at low latitudes. With this location, high-emergence latitudes are extremely difficult to achieve, since thin flux-tube simulations do not show tubes emerging at axis distances smaller than the starting distance (Granzer et al. 2000). The highest emergence latitude $b_{\rm e}$ for a given initial latitude $b_{\rm i}$ is therefore $\cos b_{\rm e} = r_{\rm cz} \cos b_{\rm i}$. An initial latitude (residence of strong dynamo fields) of 30° results in a highest emergence latitude of 46°. The largest azimuthal fields of $B_\phi^{\rm max} = 5.5$ occur at $r = 0.75$ because of the pumping, which is most efficient on stationary fields. The strongest radial surface fields are also constrained to latitudes below about 40°. We do not believe the observed high-latitude fields can be explained with this dynamo solution.

Using an isotropic α-effect with $\alpha_{rr} = \alpha_{\theta\theta} = \alpha_{\phi\phi}$ (corresponding to very slow rotation unlike AF Lep), we also obtain stationary solutions with an unchanged critical $C_\alpha = 0.20$. The Ω-effect is just much stronger in the toroidal-field equation than any of the various α-components.

The magnetic diffusivity is a relatively poorly known value in the bulk of the convection zones of the Sun and stars. We computed the dynamo solutions for two other values of $\eta_{\rm T}$, 10^{11} and 10^{13} cm^2/s, leading to $C_\Omega = 4.09 \times 10^6$ (LoEta) and $C_\Omega = 4.09 \times 10^4$ (HiEta), respectively. These diffusivities correspond to diffusion times of 1900 yr and 19 yr, again using R_* as the length scale. The ratio between rotational and meridional velocity is always kept the same. The LoEta run delivers a stationary solution as well, with a critical $C_\alpha = 0.43$. The HiEta run leads to an oscillatory solution with a critical $C_\alpha = 10.8$ – a stronger α-effect is now needed to compensate for the weaker Ω-effect. The butterfly diagram shows significant azimuthal fields at the tachocline and radial surface fields only below 60° latitude (Fig. 19).

In an attempt to increase the shear at high latitudes, we also employed a modified rotation profile that assumes that the stellar radiative interior rotates with the same velocity as the bottom of the convection zone *at the equator* (Fig. 17). All other parameters are the same as for Fig. 18. The solutions are now oscillatory, and the largest azimuthal field resides around 50° latitude (Fig. 20). Since fast rotation tends to increase the latitudes of the spot emergence as compared to the tachocline latitude of the flux (e.g., Granzer 2004), the spot latitudes from Doppler imaging may not contradict the dynamo solution. The observed spot latitudes can be a tool to probe the internal rotation of low-mass stars. The spin-down of the interior of such a young star may not have finished yet, in contrast to the Sun, where the interior rotates with a velocity seen at mid-latitudes on the surface.

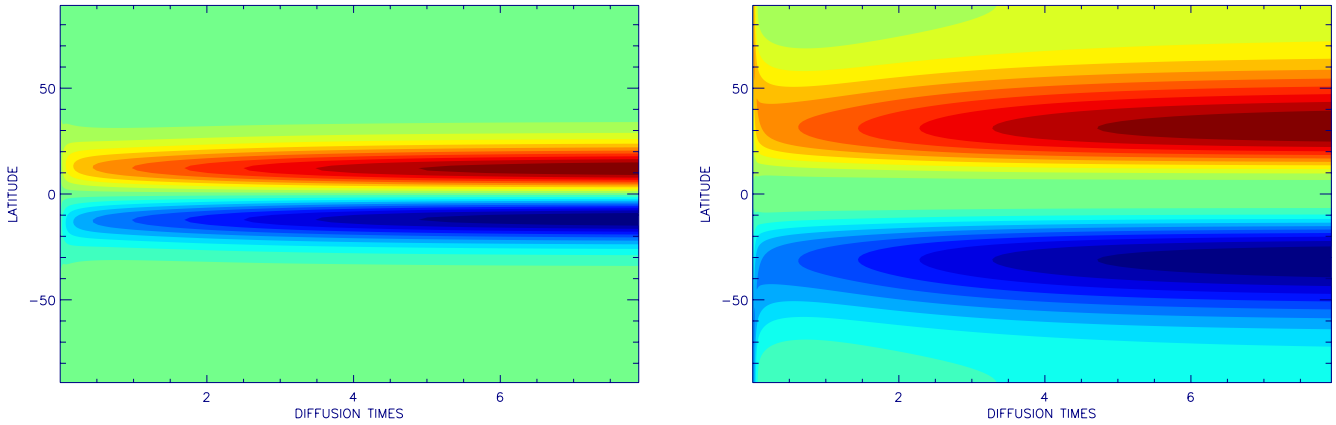

Fig. 18. Butterfly diagram for the solution with diamagnetic pumping and maximum anisotropy in α according to (5). *Left*: azimuthal magnetic field B_ϕ at a radius of $0.8R_*$ (maximum value $B_\phi^{\max} = 0.52$); *right*: radial field B_r at the stellar surface (maximum value $B_r^{\max} = 0.0007$).

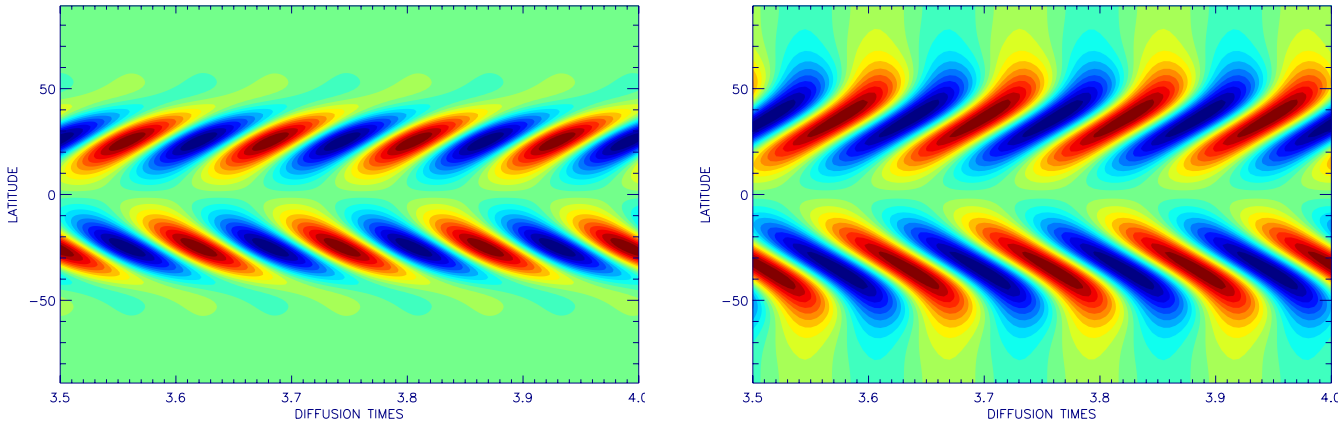

Fig. 19. As in Fig. 18, but for a magnetic diffusivity ten times higher. Maximum values are $B_\phi^{\max} = 0.052$ (*left*) and $B_r^{\max} = 0.0095$ (*right*).

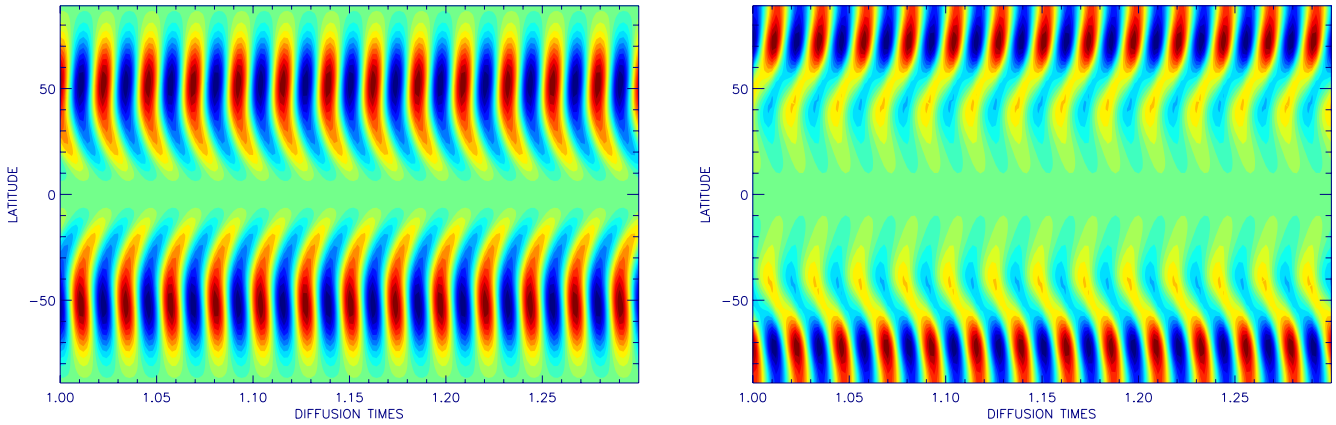

Fig. 20. As in Fig. 18, but with a fast-rotating interior (roughly equatorial surface rotation). Maximum values are $B_\phi^{\max} = 0.76$ (*left*) and $B_r^{\max} = 0.044$ (*right*).

If the value for the magnetic diffusivity is correct, the period of the cycles in Fig. 20 would be 4.5 yr. A possible cycle period of about 4 yr is indicated by the upper panel of Fig. 1 (see also Sect. 4), resulting in a full-cycle period of 8 yr including a field reversal. Given our ignorance of the exact turbulent magnetic diffusivity, the model cycle time is compatible with the observed long-term variability.

An alternative approach to the solar dynamo is the flux-transport dynamo, which is based on the Babcock-Leighton effect. It has been widely used to explain the features of the solar cycle, but is not based on theoretical consequences of the turbulence. Instead, it assumes that toroidal magnetic flux emerges from the bottom of the convection zone in a time much shorter than the cycle, and it is the tilt of bipolar sunspot groups that contributes to a near-surface poloidal magnetic field. This new poloidal flux is eventually transported down to the bottom of the convection zone by the meridional circulation. The α-term in Eq. (4) is now modified to two variants: first, to a distribution

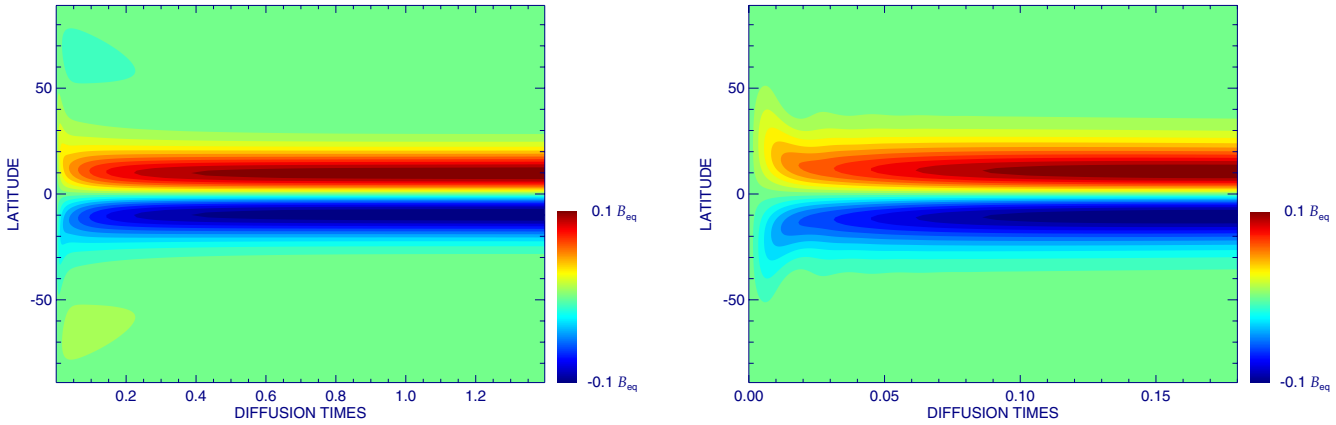

Fig. 21. Butterfly diagram for the solution with diamagnetic pumping, Babcock-Leighton-type source term for the poloidal magnetic field, and a turbulent magnetic diffusivity $\eta_T = 10^{12}$ cm^2/s. *Left*: classical solar case with a poloidal-field generation by active regions at low latitudes. *Right*: observationally driven case with a poloidal-field generation around 70° latitudes. In both cases the toroidal magnetic field at the bottom of the convection zone is plotted because this is the field relevant for spots in the Babcock-Leighton scenario.

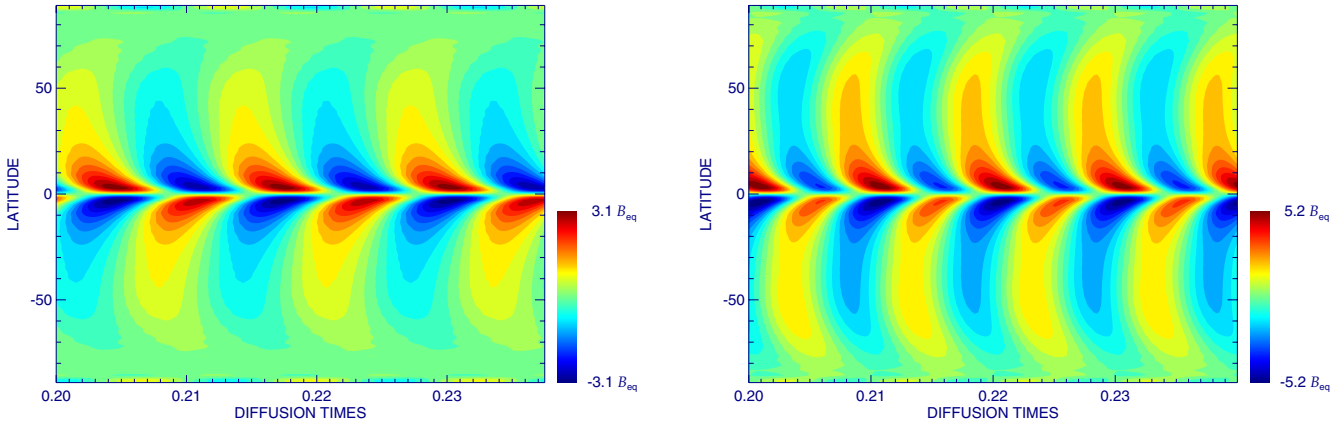

Fig. 22. Babcock-Leighton-type dynamo solutions with the same setup as in Fig. 21, but for the low turbulent magnetic diffusivity $\eta_T = 10^{11}$ cm^2/s. *Left*: classical solar case with a poloidal-field generation by active regions at low latitudes. *Right*: observationally driven case with a poloidal-field generation around 70° latitudes.

typically used in the solar case, and a distribution motivated by the presence of spots on AF Lep near 70° latitude. The α-term now reads

$$C_\alpha \psi(B_\phi^2(r_{cz},\theta))\boldsymbol{\alpha}(r,\theta) \circ \boldsymbol{B}(r_{cz},\theta) \tag{8}$$

and the α-components need to be replaced by $\alpha_{rr} = \alpha_{\theta\theta} = \alpha_{r\theta} = 0$ and

$$\alpha_{\phi\phi} = \frac{1}{2}\left[1 + \mathrm{erf}\left(\frac{r - r_s}{d}\right)\right]\cos\theta \sin^2\theta, \text{ (solar case)}$$

$$\alpha_{\phi\phi} = \frac{1}{2}\left[1 + \mathrm{erf}\left(\frac{r - r_s}{d}\right)\right]\cos\theta \sin^2\left(\left|\theta - \frac{\pi}{2}\right|^{2.5}\right), \text{ (AF Lep)}$$

where $r_s = 0.95$ restricts the poloidal-field production to a near-surface layer. These are purely geometrical descriptions; the only physical requirement is the anti-symmetry about the equator, achieved by $\cos\theta$, as was also used in the third line of Eq. (5). The main change is, however, the non-locality of this "α"-effect because it refers to the azimuthal field at the bottom of the convection zone, but acts at the surface. In contrast to solar flux-transport models, we did not restrict $\alpha_{\phi\phi}$ to low latitudes, since this restriction is motivated by the low emergence latitudes of sunspots, which does not hold here.

When employing the turbulent magnetic diffusivity of $\eta_T = 10^{12}$ cm^2/s as used in the distributed-α dynamos above, we obtain stationary solutions, as shown in Fig. 21. In both cases, the solar-type and the high-latitude Babcock-Leighton effect, the solutions are confined to low latitudes. We omit the surface radial-field plot here, since the mechanism relies on active regions forming as the result of rising flux from the toroidal field at the base of the convection zone.

A second ingredient to a Babcock-Leighton dynamo is a relatively low η_T. Figure 22 therefore shows the solutions for a value ten times lower (LoEta), resulting in $C_\Omega = 4.09 \times 10^6$. The solutions are now oscillatory. The solar case shows naturally low-latitude fields, but the high-latitude case also exhibits large toroidal fields at low latitudes, because the meridional circulation, which is equatorward at the base of the convection zone, has a stronger impact on the solutions at this low value of η_T.

Finally, we tested a fast radiative interior as we did for Fig. 20 and repeated the computations of Fig. 22. The results in Fig. 23 indicate that there is much less influence of the core rotation on the latitude of strongest toroidal fields in the Babcock-Leighton dynamo than in the distributed dynamo. Although there is a medium toroidal field up to latitudes of 60° in the right panel of Fig. 23, the much stronger fields at <10° should produce

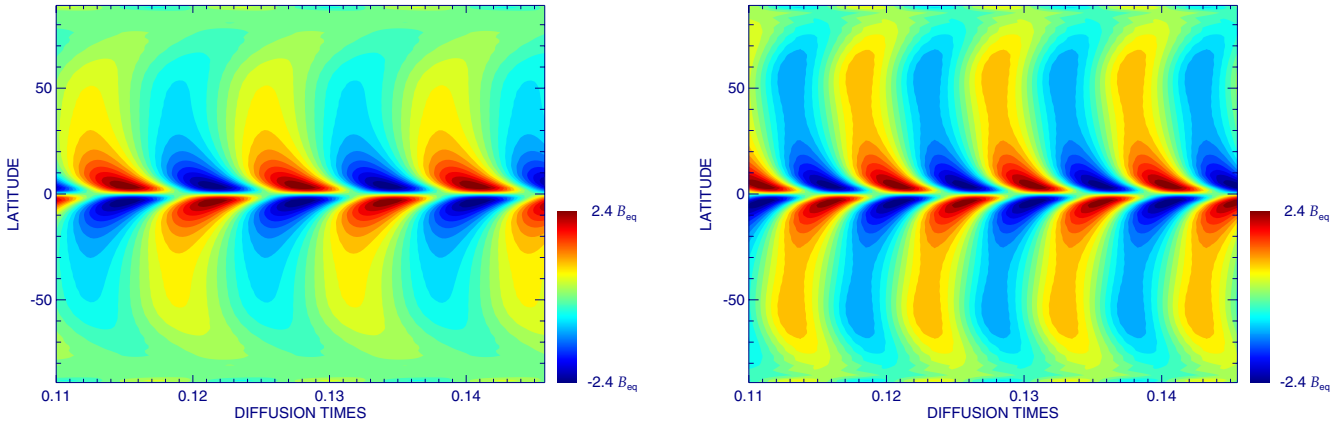

Fig. 23. Babcock-Leighton-type dynamo solutions with the same setup as in Fig. 22, but for a fast radiation zone. Again, *left*: poloidal-field generation at low latitudes, and *right*: poloidal-field generation around 70° latitudes.

a clear activity pattern not higher than 40°, even for a purely axial flux rise, which is not simulated here.

The various dynamo solutions presented here favour a distributed dynamo in the rapidly rotating convection zone of AF Lep, which gives results close to the observed spot latitudes if the radiative interior rotates as fast as the near-equator convection zone (unlike the solar radiation zone). We recall that the ZDI maps by Marsden et al. (2006) show regions of a near-surface azimuthal field, which also points to a distributed dynamo.

8. Summary and discussion

We have analysed both photometric and spectroscopic observations of the young active F dwarf AF Lep and studied whether the obtained results can be explained with theoretical models.

The long-term photometric record of AF Lep, which covers over 40 years of infrequent observations, shows that the star has become brighter over this time. While the whole period is not sufficiently sampled, the last 4.5 yr of observations are well covered and indicate a cyclic variation. The previously reported rotation period of ∼one day implied that finding the true period from ground-based observations is challenging, especially when the photometry also reveals short-term variability due to spot evolution and/or differential rotation. The photometric light curves indicate that the spot coverage can remain stable for months and then undergo several changes from month to month. With time-series analysis methods we have determined the rotation period to be 0.9660 ± 0.0023 days.

Multi-site spectroscopic observations were used to reconstruct surface temperature maps that all show a dominant high-latitude spot. This indicates that the dynamo operating in this shallow convection zone star must differ from that of the Sun. The mean longitude of the spots drifts with time, but the latitude remains relatively constant (within the accuracy of the temperature maps).

The lithium line of AF Lep shows some variability over the years. Because of the resolution (250 K) of the model calculations we cannot rule out that the variations are simply due to overall temperature fluctuations. A fluctuating Li abundance seems quite unlikely. Our results, as well as the results from others, have shown that the equivalent width of the lithium line keeps changing. However, the seasonal variations of individual equivalent-width measurements do not show any clear correlation with the phases of the spots.

We considered various dynamo solutions to produce a theoretical butterfly diagram that is comparable with the observed spot locations. A dynamo model based on a differential rotation profile in which the stellar interior rotates at the average surface angular velocity is not able to reproduce the high-latitude spots observed on AF Lep and also on other F dwarfs. However, if the stellar interior rotates with the same speed as the convection zone at the equator, it is possible to generate a substantial magnetic field at high latitudes of about 60°. Such fast internal rotation may be compatible with the young age of AF Lep. The reader is also referred to a complementary study on a more slowly rotating F-star recently published by Bonanno et al. (2014).

It is rather common that ZDI maps of the stars show the magnetic flux spread over a wide range of latitudes. Over the years, the maps have started to show more and more complex field topologies, and increasingly weaker field strengths are detected as well. Strassmeier et al. (2013) compared independent magnetic maps made by two codes from almost simultaneous observations (see Skelly et al. 2010 and Carroll et al. 2012). The disparity of the two reconstructions is noticeable. As stated by Strassmeier et al. (2013), one can only speculate about the reasons for the differences. Clearly more comparisons of the codes are needed and all reconstructions have to be interpreted with care.

Acknowledgements. This work has made use of the VALD database, operated at Uppsala University, the Institute of Astronomy RAS in Moscow, and the University of Vienna. The authors thank the anonymous referee for useful and enlightening comments and suggestions.

References

Antia, H. M., & Basu, S. 2011, ApJ, 735, L45
Barnes, J. R., Lister, T. A., Hilditch, R. W., & Collier Cameron, A. 2004, MNRAS, 348, 1321
Barnes, J. R., Collier Cameron, A., Donati, J.-F., et al. 2005a, MNRAS, 357, L1
Barnes, J. R., Collier Cameron, A., Lister, T. A., Pointer, G. R., & Still, M. D. 2005b, MNRAS, 356, 1501
Berdyugina, S. V. 1991, Bull. Crimean Astrophys. Obs., 83, 89
Berdyugina, S. V. 1998, A&A, 338, 97
Berdyugina, S. V., Pelt, J., & Tuominen, I. 2002, A&A, 394, 505
Binks, A. S., & Jeffries, R. D. 2014, MNRAS, 438, L11
Blackman, E. G., & Brandenburg, A. 2003, ApJ, 584, L99
Blackwell, D. E., & Lynas-Gray, A. E. 1994, A&A, 282, 899
Bonanno, A., Fröhlich, H.-E., Karoff, C., et al. 2014, A&A, 569, A113
Brandenburg, A., Krause, F., Meinel, R., Moss, D., & Tuominen, I. 1989, A&A, 213, 411
Budding, E., Carter, B. D., Mengel, M. W., Slee, O. B., & Donati, J.-F. 2002, PASA, 19, 527

Budding, E., Heckert, P., Soydugan, F., et al. 2003, Inform. Bull. Variable Stars, 5451, 1
Carroll, T. A., Strassmeier, K. G., Rice, J. B., & Künstler, A. 2012, A&A, 548, A95
Catala, C., Donati, J.-F., Shkolnik, E., Bohlender, D., & Alecian, E. 2007, MNRAS, 374, L42
Cole, E., Käpylä, P. J., Mantere, M. J., & Brandenburg, A. 2014, ApJ, 780, L22
Collier Cameron, A. 1995, MNRAS, 275, 534
Collier-Cameron, A., & Unruh, Y. C. 1994, MNRAS, 269, 814
Collier Cameron, A., Walter, F. M., Vilhu, O., et al. 1999, MNRAS, 308, 493
Cutispoto, G. 2002, Astron. Nachr., 323, 325
Cutispoto, G., Tagliaferri, G., Giommi, P., et al. 1991, A&AS, 87, 233
Cutispoto, G., Tagliaferri, G., Pallavicini, R., Pasquini, L., & Rodono, M. 1996, A&AS, 115, 41
Donati, J.-F., & Collier Cameron, A. 1997, MNRAS, 291, 1
Donati, J.-F., Semel, M., Carter, B. D., Rees, D. E., & Collier Cameron, A. 1997, MNRAS, 291, 658
Donati, J.-F., Collier Cameron, A., Hussain, G. A. J., & Semel, M. 1999, MNRAS, 302, 437
Donati, J.-F., Mengel, M., Carter, B. D., et al. 2000, MNRAS, 316, 699
Donati, J.-F., Collier Cameron, A., Semel, M., et al. 2003, MNRAS, 345, 1145
Donati, J.-F., Moutou, C., Farès, R., et al. 2008, MNRAS, 385, 1179
Eggen, O. J. 1986, AJ, 92, 910
Fares, R., Donati, J.-F., Moutou, C., et al. 2009, MNRAS, 398, 1383
Fekel, F. C. 1996, in Stellar Surface Structure, eds. K. G. Strassmeier, & J. L. Linsky, IAU Symp., 176, 345
Fernández, D., Figueras, F., & Torra, J. 2008, A&A, 480, 735
Granzer, T. 2004, Astron. Nachr., 325, 417
Granzer, T., Schüssler, M., Caligari, P., & Strassmeier, K. G. 2000, A&A, 355, 1087
Granzer, T., Reegen, P., & Strassmeier, K. G. 2001a, Astron. Nachr., 322, 325
Granzer, T., Weber, M., & Strassmeier, K. G. 2001b, Astron. Nachr., 322, 295
Hollerbach, R. 2000, Int. J. Num. Meth. Fluids, 32, 773
Hussain, G. A. J. 2002, Astron. Nachr., 323, 349
Hussain, G. A. J., Unruh, Y. C., & Collier Cameron, A. 1997, MNRAS, 288, 343
Järvinen, S. P., & Berdyugina, S. V. 2010, A&A, 521, A86
Jeffers, S. V., Donati, J.-F., & Collier Cameron, A. 2007, MNRAS, 375, 567
Jetsu, L., & Pelt, J. 1999, A&AS, 139, 629
Kim, Y.-C., & Demarque, P. 1996, ApJ, 457, 340
Kitchatinov, L. L., & Olemskoy, S. V. 2012, Sol. Phys., 276, 3
Kitchatinov, L. L., & Rüdiger, G. 2005, Astron. Nachr., 326, 379
Kitchatinov, L. L., Ruediger, G., & Kueker, M. 1994, A&A, 292, 125
Krause, F., & Rädler, K. H. 1980, Mean-field magnetohydrodynamics and dynamo theory
Kürster, M., Schmitt, J. H. M. M., & Cutispoto, G. 1994, A&A, 289, 899
Küker, M., & Rüdiger, G. 2007, Astron. Nachr., 328, 1050
Küker, M., & Rüdiger, G. 2011, Astron. Nachr., 332, 933
Küker, M., Ruediger, G., & Kitchatinov, L. L. 1993, A&A, 279, L1
Küker, M., Rüdiger, G., & Schultz, M. 2001, A&A, 374, 301
Kupka, F., Piskunov, N., Ryabchikova, T. A., Stempels, H. C., & Weiss, W. W. 1999, A&AS, 138, 119
Kurucz, R. 1993, ATLAS9 Stellar Atmosphere Programs and 2 km s^{-1} grid. Kurucz CD-ROM No. 13. Cambridge, Mass.: Smithsonian Astrophysical Observatory, 13
Lanza, A. F. 2011, in IAU Symp. 273, eds. D. Prasad Choudhary, & K. G. Strassmeier, 89
Lanza, A. F., Pagano, I., Leto, G., et al. 2009, A&A, 493, 193
Lehtinen, J., Jetsu, L., Hackman, T., Kajatkari, P., & Henry, G. W. 2011, A&A, 527, A136
Lister, T. A., Collier Cameron, A., & Bartus, J. 1999, MNRAS, 307, 685
Maceroni, C., van't Veer, F., & Vilhu, O. 1991, The Messenger, 66, 47
Maceroni, C., Vilhu, O., van't Veer, F., & van Hamme, W. 1994, A&A, 288, 529
Mamajek, E. E., & Bell, C. P. M. 2014, MNRAS, 445, 2169
Marsden, S. C., Waite, I. A., Carter, B. D., & Donati, J.-F. 2004, Astron. Nachr., 325, 246
Marsden, S. C., Waite, I. A., Carter, B. D., & Donati, J.-F. 2005, MNRAS, 359, 711
Marsden, S. C., Mengel, M. W., Donati, F., et al. 2006, in ASP Conf. Ser. 358, eds. R. Casini, & B. W. Lites, 401
Marsden, S. C., Jardine, M. M., Ramírez Vélez, J. C., et al. 2011a, MNRAS, 413, 1922
Marsden, S. C., Jardine, M. M., Ramírez Vélez, J. C., et al. 2011b, MNRAS, 413, 1939
Meibom, S., Mathieu, R. D., Stassun, K. G., Liebesny, P., & Saar, S. H. 2011, ApJ, 733, 115
Mentuch, E., Brandeker, A., van Kerkwijk, M. H., Jayawardhana, R., & Hauschildt, P. H. 2008, ApJ, 689, 1127
Moss, D., Barker, D. M., Brandenburg, A., & Tuominen, I. 1995, A&A, 294, 155
Mosser, B., Baudin, F., Lanza, A. F., et al. 2009, A&A, 506, 245
Pallavicini, R., Cutispoto, G., Randich, S., & Gratton, R. 1993, A&A, 267, 145
Passos, D., Nandy, D., Hazra, S., & Lopes, I. 2014, A&A, 563, A18
Paxton, B., Bildsten, L., Dotter, A., et al. 2011, ApJS, 192, 3
Piluso, N., Lanza, A. F., Pagano, I., Lanzafame, A. C., & Donati, J.-F. 2008, MNRAS, 387, 237
Piskunov, N. E., Kupka, F., Ryabchikova, T. A., Weiss, W. W., & Jeffery, C. S. 1995, A&AS, 112, 525
Press, W. H., Teukolsky, S. A., Vetterling, W. T., & Flannery, B. P. 1992, Numerical recipes in Fortran, The art of scientific computing
Reinhold, T., Reiners, A., & Basri, G. 2013, A&A, 560, A4
Rüdiger, G. 1989, Differential rotation and stellar convection. Sun and the solar stars
Semel, M. 1989, A&A, 225, 456
Semel, M., Donati, J.-F., & Rees, D. E. 1993, A&A, 278, 231
Silva-Valio, A. 2008, ApJ, 683, L179
Silva-Valio, A., Lanza, A. F., Alonso, R., & Barge, P. 2010, A&A, 510, A25
Skelly, M. B., Donati, J.-F., Bouvier, J., et al. 2010, MNRAS, 403, 159
Solanki, S. K. 2003, A&ARv, 11, 153
Stokes, N. R. 1972, MNRAS, 159, 165
Stout-Batalha, N. M., & Vogt, S. S. 1999, ApJS, 123, 251
Strassmeier, K. G. 2009, A&ARv, 17, 251
Strassmeier, K. G., & Rice, J. B. 2003, A&A, 399, 315
Strassmeier, K. G., Bartus, J., Cutispoto, G., & Rodono, M. 1997a, A&AS, 125, 11
Strassmeier, K. G., Boyd, L. J., Epand, D. H., & Granzer, T. 1997b, PASP, 109, 697
Strassmeier, K. G., Granzer, T., Weber, M., et al. 2004, Astron. Nachr., 325, 527
Strassmeier, K. G., Carroll, T. A., Ilyin, I., & Järvinen, S. 2013, in IAU Symp. 294, eds. A. G. Kosovichev, E. de Gouveia Dal Pino, & Y. Yan, 447
Tagliaferri, G., Cutispoto, G., Pallavicini, R., Randich, S., & Pasquini, L. 1994, A&A, 285, 272
Unruh, Y. C., & Collier Cameron, A. 1997, MNRAS, 290, L37
Unruh, Y. C., Collier Cameron, A., & Cutispoto, G. 1995, MNRAS, 277, 1145
Warnecke, J., Brandenburg, A., & Mitra, D. 2011, A&A, 534, A11
Weise, P., Launhardt, R., Setiawan, J., & Henning, T. 2010, A&A, 517, A88
White, R. J., Gabor, J. M., & Hillenbrand, L. A. 2007, AJ, 133, 2524
Wichmann, R., Schmitt, J. H. M. M., & Hubrig, S. 2003, A&A, 399, 983

Pages 13 to 18 are available in the electronic edition of the journal at http://www.aanda.org

Table 1. Spectroscopic observations of AF Lep with SES at the STELLA observatory.

HJD 2 450 000+	Day	Phase	S/N	Exp. t s	HJD 2 450 000+	Day	Phase	S/N	Exp. t s
	2008				5168.581883	03/12/2009	0.85	119	1200
4806.449041	05/12/2008	0.97	84	1200	5168.612782	03/12/2009	0.88	92	1200
4806.488960	05/12/2008	0.01	69	1200	5168.651441	03/12/2009	0.92	113	1200
4807.442635	06/12/2008	1.00	68	1144	5168.684299	03/12/2009	0.95	88	1200
4807.485140	06/12/2008	0.04	75	1200	5168.724356	03/12/2009	1.00	71	1200
4807.500198	06/12/2008	0.06	71	1200	5169.677176	04/12/2009	0.98	93	1200
4808.455330	07/12/2008	0.05	92	1200	5169.706822	04/12/2009	0.01	74	1200
4808.506302	07/12/2008	0.10	91	1200		*2010*			
4808.686498	08/12/2008	0.29	95	1200	5210.375680	13/01/2010	0.11	107	1200
4809.455377	08/12/2008	0.08	91	1200	5210.481473	13/01/2010	0.22	113	1200
4809.514308	09/12/2008	0.14	79	1200	5210.510337	13/01/2010	0.25	113	1200
	2009				5210.615744	14/01/2010	0.36	70	1200
5163.435205	27/11/2009	0.52	85	1200	5211.432112	14/01/2010	0.21	123	1200
5163.452347	27/11/2009	0.54	81	1200	5211.468481	14/01/2010	0.24	126	1200
5163.485338	27/11/2009	0.57	100	1200	5211.503232	14/01/2010	0.28	121	1200
5163.513160	28/11/2009	0.60	93	1200	5211.542212	15/01/2010	0.32	136	1200
5163.552318	28/11/2009	0.64	92	1200	5211.570609	15/01/2010	0.35	125	1200
5163.580713	28/11/2009	0.67	101	1200	5211.600474	15/01/2010	0.38	89	1200
5163.612288	28/11/2009	0.70	106	1200	5212.416273	15/01/2010	0.22	121	1200
5163.640174	28/11/2009	0.73	85	1200	5212.456635	15/01/2010	0.27	125	1200
5163.672249	28/11/2009	0.77	102	1200	5212.489709	15/01/2010	0.30	128	807
5163.700904	28/11/2009	0.79	90	1200	5212.566831	16/01/2010	0.38	133	1200
5163.736466	28/11/2009	0.83	63	1200	5212.606046	16/01/2010	0.42	97	1200
5164.503297	28/11/2009	0.63	94	1200	5213.412320	16/01/2010	0.26	99	1200
5164.640697	29/11/2009	0.77	86	1200	5213.455694	16/01/2010	0.30	116	1200
5164.674109	29/11/2009	0.80	106	1200	5213.499864	16/01/2010	0.35	103	1200
5165.457987	29/11/2009	0.61	90	1200	5213.541172	17/01/2010	0.39	109	1200
5165.499258	29/11/2009	0.66	97	1200	5213.569589	17/01/2010	0.42	119	1200
5165.529145	30/11/2009	0.69	99	1200	5214.413196	17/01/2010	0.29	91	1200
5165.568430	30/11/2009	0.73	93	1200	5214.450284	17/01/2010	0.33	92	1200
5165.596842	30/11/2009	0.76	76	1200	5214.484901	17/01/2010	0.37	100	1200
5165.625225	30/11/2009	0.79	99	1200	5214.513877	18/01/2010	0.40	97	1200
5165.652971	30/11/2009	0.82	92	1200	5214.561562	18/01/2010	0.45	80	1200
5165.680734	30/11/2009	0.84	97	1200	5214.594582	18/01/2010	0.48	55	1200
5165.718373	30/11/2009	0.88	65	1200	5215.332572	18/01/2010	0.24	79	555
5166.658329	01/12/2009	0.86	67	828	5215.370475	18/01/2010	0.28	36	300
5167.459250	01/12/2009	0.69	88	1200	5215.482607	18/01/2010	0.40	122	1200
5167.487761	01/12/2009	0.72	88	1200	5215.524929	19/01/2010	0.44	132	1200
5167.521360	02/12/2009	0.75	104	1200	5215.576123	19/01/2010	0.50	126	1200
5167.644374	02/12/2009	0.88	104	1200	5216.414315	19/01/2010	0.36	132	1200
5167.686452	02/12/2009	0.92	81	1200	5216.443441	19/01/2010	0.39	127	1200
5167.716547	02/12/2009	0.95	89	1200	5216.479376	19/01/2010	0.43	109	1200
5168.430527	02/12/2009	0.69	78	1200	5216.520433	20/01/2010	0.47	74	1200
5168.463362	02/12/2009	0.73	84	1200	5216.569482	20/01/2010	0.52	125	1200
5168.496477	02/12/2009	0.76	93	1200	5216.597955	20/01/2010	0.55	96	1200
5168.550220	03/12/2009	0.81	117	1200					

Notes. The S/N given is an average value for spectral region 4750–6900 Å.

Table 2. Spectroscopic observations of AF Lep with SemelPol at the AAT.

HJD 2 450 000+	Day	Phase	S/N	Exp. t s	HJD 2 450 000+	Day	Phase	S/N	Exp. t s
	2008				4814.968	14/12/2008	0.79	100	400
4806.107	05/12/2008	0.61	25	400	4814.974	14/12/2008	0.79	100	400
4806.113	05/12/2008	0.62	26	400	4814.979	14/12/2008	0.80	100	400
4806.118	05/12/2008	0.63	61	400	4814.985	14/12/2008	0.81	100	400
4806.124	05/12/2008	0.63	32	400	4815.053	14/12/2008	0.88	96	400
4806.130	05/12/2008	0.64	25	400	4815.059	14/12/2008	0.88	100	400
4806.135	05/12/2008	0.64	70	400	4815.065	14/12/2008	0.89	100	400
4806.141	05/12/2008	0.65	60	400	4815.070	14/12/2008	0.89	100	400
4806.147	05/12/2008	0.66	67	400	4815.124	14/12/2008	0.95	110	400
4806.153	05/12/2008	0.66	54	400	4815.130	14/12/2008	0.96	120	400
4806.158	05/12/2008	0.67	26	400	4815.141	14/12/2008	0.97	100	400
4806.164	05/12/2008	0.67	53	400	4816.078	15/12/2008	0.94	190	400
4806.169	05/12/2008	0.68	40	400	4816.083	15/12/2008	0.94	190	400
4806.175	05/12/2008	0.69	26	400	4816.089	15/12/2008	0.95	190	400
4806.181	05/12/2008	0.69	21	400	4816.095	15/12/2008	0.95	190	400
4806.220	05/12/2008	0.73	77	400	4816.169	15/12/2008	0.03	160	400
4806.226	05/12/2008	0.74	69	400	4816.175	15/12/2008	0.04	160	400
4806.254	05/12/2008	0.77	45	400	4816.180	15/12/2008	0.04	170	400
4806.260	05/12/2008	0.77	67	400	4816.186	15/12/2008	0.05	160	400
4808.033	07/12/2008	0.61	75	400	4817.110	16/12/2008	0.01	180	400
4808.039	07/12/2008	0.61	100	400	4817.115	16/12/2008	0.01	180	400
4808.045	07/12/2008	0.62	100	400	4817.121	16/12/2008	0.02	180	400
4808.050	07/12/2008	0.63	29	400	4817.127	16/12/2008	0.02	180	400
4808.055	07/12/2008	0.63	28	400	4817.178	16/12/2008	0.08	140	400
4809.015	08/12/2008	0.63	160	400	4817.184	16/12/2008	0.08	130	400
4809.020	08/12/2008	0.63	140	400	4817.190	16/12/2008	0.09	130	400
4809.026	08/12/2008	0.64	160	400	4817.195	16/12/2008	0.09	130	400
4809.032	08/12/2008	0.64	150	400	4817.933	17/12/2008	0.86	110	400
4809.128	08/12/2008	0.74	160	400	4817.938	17/12/2008	0.86	120	400
4809.134	08/12/2008	0.75	170	400	4817.944	17/12/2008	0.87	110	400
4809.139	08/12/2008	0.75	160	400	4817.950	17/12/2008	0.87	100	400
4809.145	08/12/2008	0.76	170	400	4818.024	17/12/2008	0.95	130	400
4809.197	08/12/2008	0.81	130	400	4818.041	17/12/2008	0.97	100	400
4809.203	08/12/2008	0.82	150	400	4818.130	17/12/2008	0.06	130	400
4809.208	08/12/2008	0.82	140	400	4818.136	17/12/2008	0.07	94	400
4809.214	08/12/2008	0.83	130	400	4818.141	17/12/2008	0.07	120	400
4809.962	09/12/2008	0.61	110	400	4818.147	17/12/2008	0.08	130	400
4809.968	09/12/2008	0.61	120	400	4818.153	17/12/2008	0.08	150	400
4809.974	09/12/2008	0.62	120	400	4818.158	17/12/2008	0.09	150	400
4809.979	09/12/2008	0.62	130	400	4818.164	17/12/2008	0.10	140	400
4810.966	10/12/2008	0.64	95	400	4818.170	17/12/2008	0.10	130	400
4810.971	10/12/2008	0.65	100	400	4818.913	18/12/2008	0.87	76	400
4810.977	10/12/2008	0.66	140	400	4818.919	18/12/2008	0.88	99	400
4810.983	10/12/2008	0.66	110	400	4818.925	18/12/2008	0.88	88	400
4810.988	10/12/2008	0.67	110	400	4818.930	18/12/2008	0.89	98	400
4810.994	10/12/2008	0.67	140	400	4818.936	18/12/2008	0.90	100	400
4811.000	10/12/2008	0.68	140	400	4818.942	18/12/2008	0.90	120	400
4811.005	10/12/2008	0.69	100	400	4818.947	18/12/2008	0.91	120	400
4811.058	10/12/2008	0.74	120	400	4818.953	18/12/2008	0.91	110	400
4811.064	10/12/2008	0.75	150	400	4818.959	18/12/2008	0.92	50	400
4811.070	10/12/2008	0.75	160	400	4818.964	18/12/2008	0.92	80	400
4811.075	10/12/2008	0.76	160	400	4818.976	18/12/2008	0.94	110	400
4811.175	10/12/2008	0.86	180	400	4818.982	18/12/2008	0.94	120	400
4811.180	10/12/2008	0.87	190	400	4818.987	18/12/2008	0.95	110	400
4811.186	10/12/2008	0.87	180	400	4818.993	18/12/2008	0.95	41	400
4811.192	10/12/2008	0.88	170	400	4818.999	18/12/2008	0.96	61	400
4811.260	10/12/2008	0.95	130	400	4819.005	18/12/2008	0.97	110	400
4811.266	10/12/2008	0.96	130	400	4819.010	18/12/2008	0.97	120	400
4811.272	10/12/2008	0.96	110	400	4819.016	18/12/2008	0.98	140	400
4819.021	18/12/2008	0.98	150	400	5163.975	28/11/2009	0.08	110	400
4819.081	18/12/2008	0.05	130	400	5163.981	28/11/2009	0.08	130	400
4819.087	18/12/2008	0.05	150	400	5163.987	28/11/2009	0.09	120	400
4819.093	18/12/2008	0.06	170	400	5163.992	28/11/2009	0.10	130	400

Notes. The S/N given is an average value for spectral region 4750–6900 Å.

Table 2. continued.

HJD 2 450 000+	Day	Phase	S/N	Exp. t s	HJD 2 450 000+	Day	Phase	S/N	Exp. t s
4819.098	18/12/2008	0.06	160	400	5164.079	28/11/2009	0.19	150	400
4819.104	18/12/2008	0.07	160	400	5164.085	28/11/2009	0.19	170	400
4819.110	18/12/2008	0.08	150	400	5164.091	28/11/2009	0.20	160	400
4819.115	18/12/2008	0.08	170	400	5164.096	28/11/2009	0.20	150	400
4819.121	18/12/2008	0.09	160	400	5164.102	28/11/2009	0.21	150	400
4819.174	18/12/2008	0.14	100	400	5164.108	28/11/2009	0.22	160	400
4819.180	18/12/2008	0.15	99	400	5164.113	28/11/2009	0.22	140	400
4819.186	18/12/2008	0.15	100	400	5164.119	28/11/2009	0.23	160	400
4819.191	18/12/2008	0.16	110	400	5164.205	28/11/2009	0.32	150	400
4819.197	18/12/2008	0.17	110	400	5164.210	28/11/2009	0.32	160	400
4819.203	18/12/2008	0.17	99	400	5164.216	28/11/2009	0.33	130	400
4819.208	18/12/2008	0.18	110	400	5164.221	28/11/2009	0.33	150	400
4819.214	18/12/2008	0.18	99	400	5164.227	28/11/2009	0.34	140	400
	2009				5164.233	28/11/2009	0.35	150	400
5160.988	25/11/2009	0.99	96	400	5164.238	28/11/2009	0.35	150	400
5160.994	25/11/2009	0.99	110	400	5164.244	28/11/2009	0.36	150	400
5160.999	25/11/2009	1.00	130	400	5164.250	28/11/2009	0.36	150	400
5161.005	25/11/2009	0.00	89	400	5164.256	28/11/2009	0.37	130	400
5161.011	25/11/2009	0.01	100	400	5164.261	28/11/2009	0.37	120	400
5161.016	25/11/2009	0.02	130	400	5164.959	29/11/2009	0.10	120	400
5161.028	25/11/2009	0.03	92	400	5164.965	29/11/2009	0.10	130	400
5161.074	25/11/2009	0.08	170	400	5164.971	29/11/2009	0.11	120	400
5161.079	25/11/2009	0.08	160	400	5164.976	29/11/2009	0.11	130	400
5161.085	25/11/2009	0.09	170	400	5164.982	29/11/2009	0.12	110	400
5161.091	25/11/2009	0.09	140	400	5164.988	29/11/2009	0.13	120	400
5161.214	25/11/2009	0.22	140	400	5164.993	29/11/2009	0.13	120	400
5161.220	25/11/2009	0.23	140	400	5164.999	29/11/2009	0.14	110	400
5161.225	25/11/2009	0.23	140	400	5165.086	29/11/2009	0.23	120	400
5161.231	25/11/2009	0.24	150	400	5165.091	29/11/2009	0.23	120	400
5162.963	27/11/2009	0.03	150	400	5165.097	29/11/2009	0.24	120	400
5162.969	27/11/2009	0.04	150	400	5165.103	29/11/2009	0.25	120	400
5162.974	27/11/2009	0.04	160	400	5165.108	29/11/2009	0.25	100	400
5162.980	27/11/2009	0.05	160	400	5165.120	29/11/2009	0.26	120	400
5162.986	27/11/2009	0.05	160	400	5165.125	29/11/2009	0.27	120	400
5162.991	27/11/2009	0.06	160	400	5165.211	29/11/2009	0.36	110	400
5162.997	27/11/2009	0.07	160	400	5165.216	29/11/2009	0.36	100	400
5163.003	27/11/2009	0.07	160	400	5165.222	29/11/2009	0.37	120	400
5163.089	27/11/2009	0.16	180	400	5165.228	29/11/2009	0.38	120	400
5163.094	27/11/2009	0.17	170	400	5165.233	29/11/2009	0.38	120	400
5163.100	27/11/2009	0.17	170	400	5165.239	29/11/2009	0.39	110	400
5163.106	27/11/2009	0.18	170	400	5165.245	29/11/2009	0.39	100	400
5163.112	27/11/2009	0.19	180	400	5165.250	29/11/2009	0.40	110	400
5163.117	27/11/2009	0.19	190	400	5166.048	30/11/2009	0.22	89	400
5163.123	27/11/2009	0.20	200	400	5166.054	30/11/2009	0.23	92	400
5163.128	27/11/2009	0.20	210	400	5166.059	30/11/2009	0.24	94	400
5163.213	27/11/2009	0.29	180	400	5166.065	30/11/2009	0.24	71	400
5163.219	27/11/2009	0.30	180	400	5166.208	30/11/2009	0.39	98	400
5163.225	27/11/2009	0.31	180	400	5166.214	30/11/2009	0.40	100	400
5163.230	27/11/2009	0.31	180	400	5166.219	30/11/2009	0.40	110	400
5163.236	27/11/2009	0.32	170	400	5166.225	30/11/2009	0.41	110	400
5163.242	27/11/2009	0.32	170	400	5166.231	30/11/2009	0.41	100	400
5163.247	27/11/2009	0.33	170	400	5166.987	01/12/2009	0.20	170	400
5163.253	27/11/2009	0.33	170	400	5166.993	01/12/2009	0.20	170	400
5163.958	28/11/2009	0.06	100	400	5166.999	01/12/2009	0.21	170	400
5163.964	28/11/2009	0.07	110	400	5167.004	01/12/2009	0.21	170	400
5163.970	28/11/2009	0.07	110	400	5167.010	01/12/2009	0.22	160	400
5167.016	01/12/2009	0.23	160	400	5168.247	02/12/2009	0.50	170	400
5167.021	01/12/2009	0.23	150	400	5168.252	02/12/2009	0.51	160	400
5167.027	01/12/2009	0.24	150	400	5168.258	02/12/2009	0.51	160	400
5167.120	01/12/2009	0.33	150	400	5168.966	03/12/2009	0.25	100	400
5167.126	01/12/2009	0.34	150	400	5168.972	03/12/2009	0.25	110	400
5167.131	01/12/2009	0.35	150	400	5168.978	03/12/2009	0.26	110	400
5167.137	01/12/2009	0.35	150	400	5168.983	03/12/2009	0.26	110	400
5167.143	01/12/2009	0.36	140	400	5168.989	03/12/2009	0.27	120	400
5167.148	01/12/2009	0.36	120	400	5168.995	03/12/2009	0.28	130	400

Table 2. continued.

HJD 2 450 000+	Day	Phase	S/N	Exp. t s	HJD 2 450 000+	Day	Phase	S/N	Exp. t s
5167.154	01/12/2009	0.37	110	400	5169.000	03/12/2009	0.28	130	400
5167.159	01/12/2009	0.37	110	400	5169.006	03/12/2009	0.29	130	400
5167.248	01/12/2009	0.47	110	400	5169.094	03/12/2009	0.38	160	400
5167.254	01/12/2009	0.47	110	400	5169.099	03/12/2009	0.38	170	400
5167.259	01/12/2009	0.48	120	400	5169.105	03/12/2009	0.39	170	400
5167.265	01/12/2009	0.48	120	400	5169.111	03/12/2009	0.40	170	400
5167.970	02/12/2009	0.21	150	400	5169.116	03/12/2009	0.40	140	400
5167.976	02/12/2009	0.22	150	400	5169.122	03/12/2009	0.41	130	400
5167.981	02/12/2009	0.23	160	400	5169.128	03/12/2009	0.41	130	400
5167.987	02/12/2009	0.23	160	400	5169.133	03/12/2009	0.42	140	400
5168.072	02/12/2009	0.32	150	400	5169.226	03/12/2009	0.51	110	400
5168.078	02/12/2009	0.33	150	400	5169.231	03/12/2009	0.52	110	400
5168.083	02/12/2009	0.33	150	400	5169.237	03/12/2009	0.53	150	400
5168.089	02/12/2009	0.34	160	400	5169.243	03/12/2009	0.53	140	400
5168.095	02/12/2009	0.34	160	400	5169.249	03/12/2009	0.54	130	400
5168.100	02/12/2009	0.35	150	400	5169.254	03/12/2009	0.54	140	400
5168.106	02/12/2009	0.36	150	400	5169.260	03/12/2009	0.55	140	400
5168.112	02/12/2009	0.36	150	400	5169.265	03/12/2009	0.56	110	400
5168.241	02/12/2009	0.49	170	400					

Table 3. Spectroscopic observations of AF Lep with SOFIN at the Nordic Optical Telescope.

HJD 2 450 000+	Day	Phase	S/N	Exp. t s	HJD 2 450 000+	Day	Phase	S/N	Exp. t s
	2005				3692.770714	18/11/2005	0.09	202	331
3684.618998	10/11/2005	0.65	277	907	3693.576113	19/11/2005	0.93	296	600
3685.665527	11/11/2005	0.74	190	900	3693.582053	19/11/2005	0.93	132	167
3685.673962	11/11/2005	0.75	127	300	3695.574304	21/11/2005	1.00	219	600
3687.697405	13/11/2005	0.84	179	900	3695.582746	21/11/2005	0.00	257	600
3687.709327	13/11/2005	0.85	207	900	3695.773502	21/11/2005	0.20	178	420
3691.572759	17/11/2005	0.85	267	676	3695.779279	21/11/2005	0.20	155	317
3692.584815	18/11/2005	0.90	254	651	3696.641835	22/11/2005	0.10	229	780
3692.764852	18/11/2005	0.09	259	423	3696.652217	22/11/2005	0.11	231	754

Notes. The S/N given is for spectral region around 6430 Å.

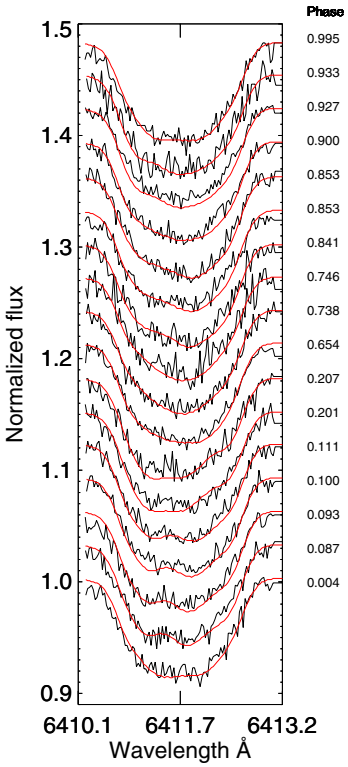

Fig. 7. Calculated (red line) and observed (black line) spectral lines for 2005.87 data set using Fe I 6411.64 Å line.

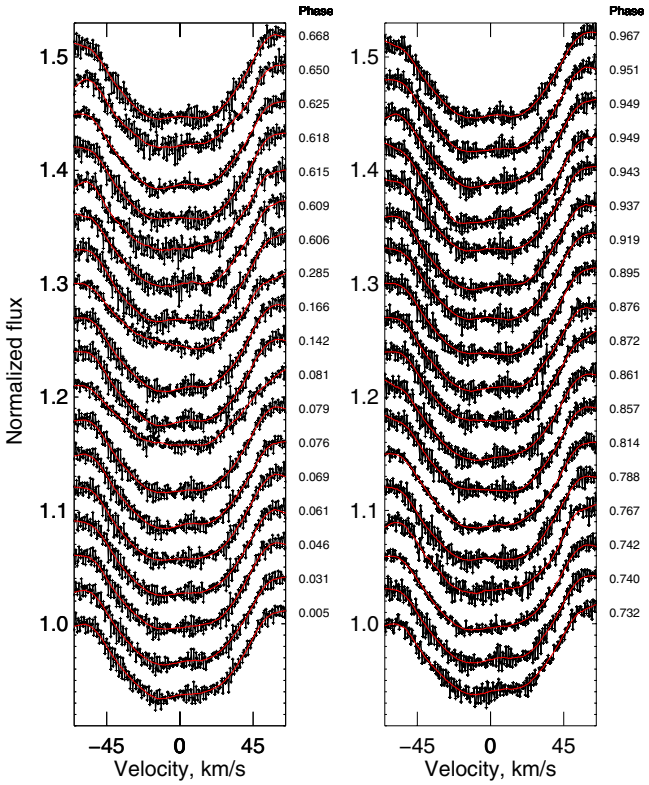

Fig. 8. Calculated (red line) and observed (black line) LSD profiles for 2008.95 data set.

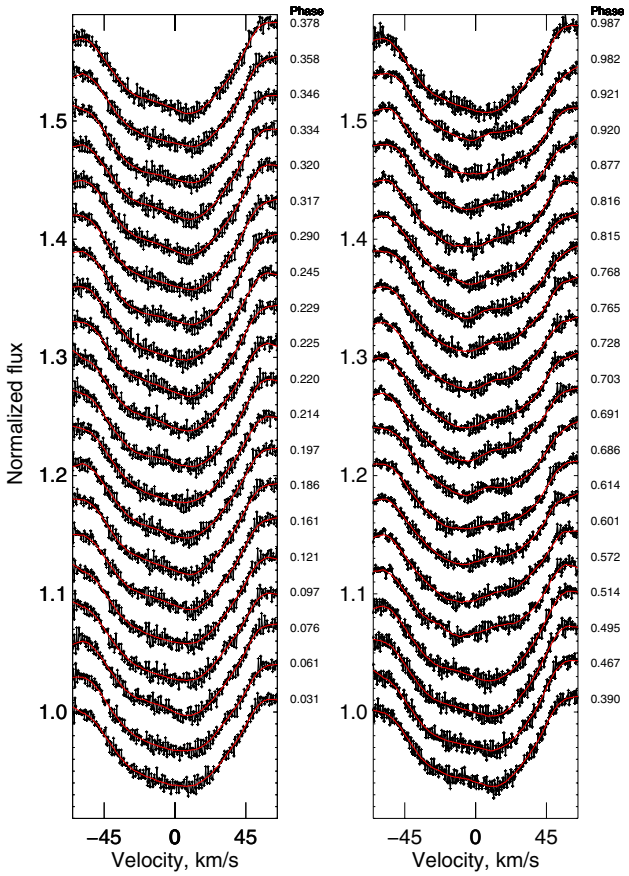

Fig. 9. Calculated (red line) and observed (black line) LSD profiles for 2009.92 data set.

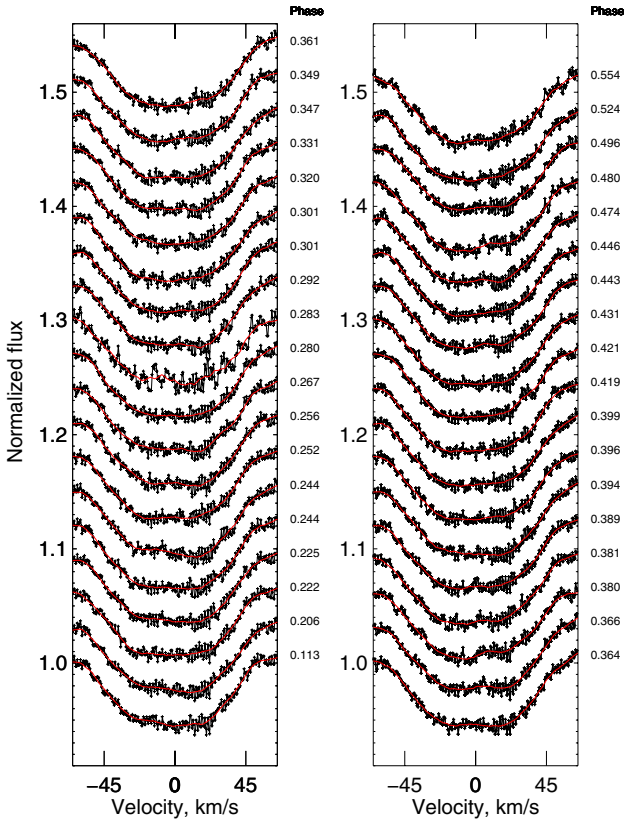

Fig. 10. Calculated (red line) and observed (black line) LSD profiles for 2010.04 data set.

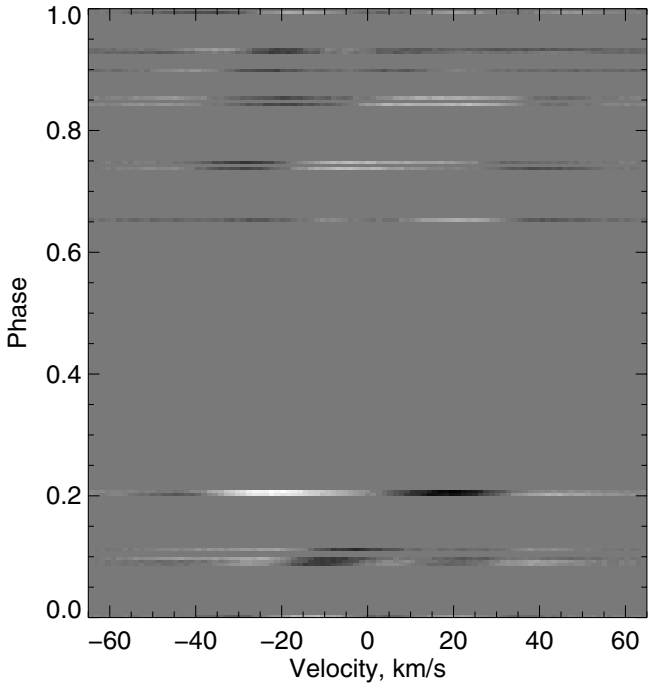

Fig. 11. Difference between the mean profile and the observed profile for 2005 data to show the movements of the spots through line profiles as a function of phase. The darker colour indicates the presence of a spot.

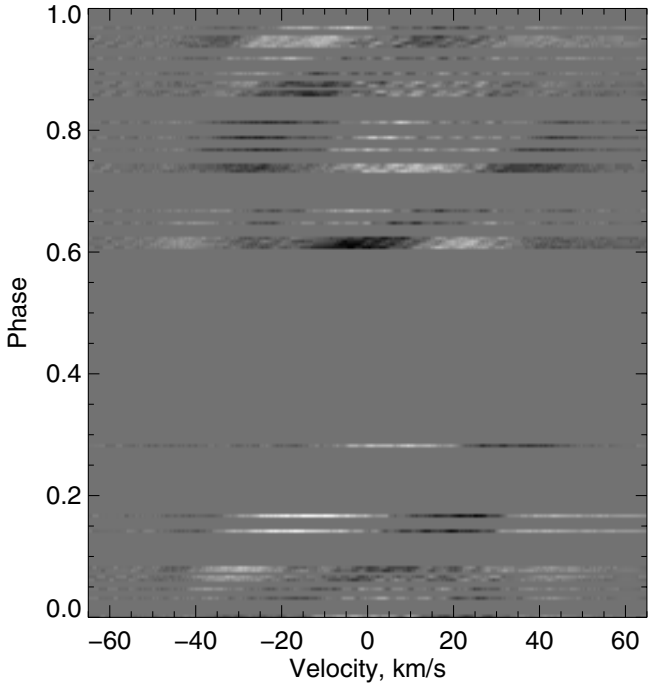

Fig. 12. As Fig. 11 but for 2008 data.

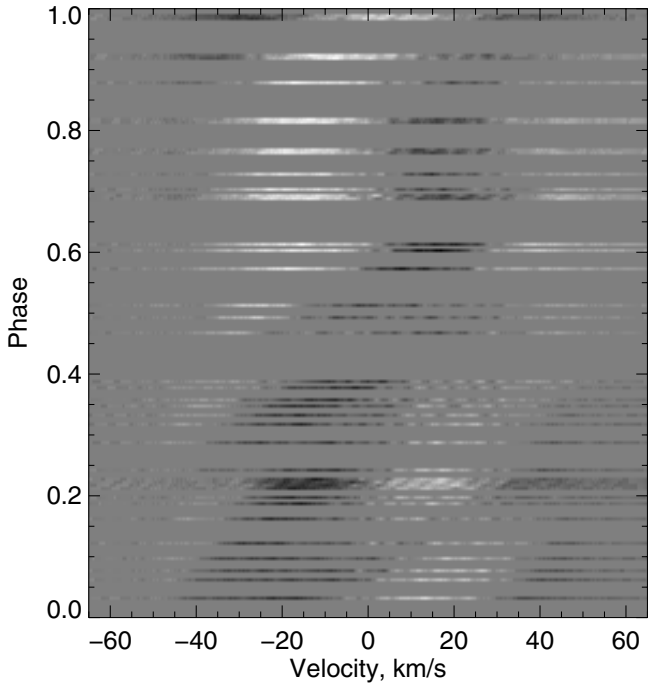

Fig. 13. As Fig. 11 but for 2009 data.

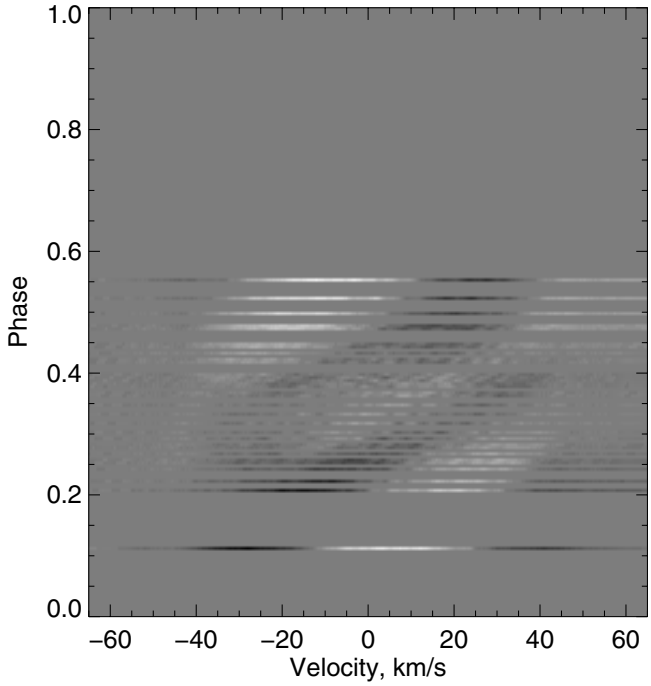

Fig. 14. As Fig. 11 but for 2010 data.